



AFRL-AFOSR-UK-TR-2015-0035



## **Investigating the catalytic growth of carbon nanotubes with in situ Raman monitoring**

**Vincent Jourdain**

**CTRE NAT DE LA RECHERCHE SCIENTIFIQUE  
1919, ROUTE DE MENDE  
MONTPELLIER, 34000 FRANCE**

**EOARD Grant #FA8655-12-1-2059**

**Report Date: June 2015**

**Final Report from 1 April 2012 to 31 March 2015**

**Distribution Statement A: Approved for public release distribution is unlimited.  
COPYRIGHT MATERIAL WITH GOVERNMENT PURPOSE RIGHTS**

**Air Force Research Laboratory  
Air Force Office of Scientific Research  
European Office of Aerospace Research and Development  
Unit 4515, APO AE 09421-4515**

**REPORT DOCUMENTATION PAGE**
*Form Approved  
OMB No. 0704-0188*

The public reporting burden for this collection of information is estimated to average 1 hour per response, including the time for reviewing instructions, searching existing data sources, gathering and maintaining the data needed, and completing and reviewing the collection of information. Send comments regarding this burden estimate or any other aspect of this collection of information, including suggestions for reducing the burden, to Department of Defense, Washington Headquarters Services, Directorate for Information Operations and Reports (0704-0188), 1215 Jefferson Davis Highway, Suite 1204, Arlington, VA 22202-4302. Respondents should be aware that notwithstanding any other provision of law, no person shall be subject to any penalty for failing to comply with a collection of information if it does not display a currently valid OMB control number.

**PLEASE DO NOT RETURN YOUR FORM TO THE ABOVE ADDRESS.**

1. REPORT DATE (DD-MM-YYYY) 06/11/2015	2. REPORT TYPE Final	3. DATES COVERED (From - To) 20120401-20150331		
4. TITLE AND SUBTITLE Investigating the catalytic growth of carbon nanotubes with in situ Raman monitoring		5a. CONTRACT NUMBER		
		5b. GRANT NUMBER FA8655-12-1-2059		
		5c. PROGRAM ELEMENT NUMBER 61102F		
6. AUTHOR(S) Vincent Jourdain		5d. PROJECT NUMBER		
		5e. TASK NUMBER		
		5f. WORK UNIT NUMBER		
7. PERFORMING ORGANIZATION NAME(S) AND ADDRESS(ES) CTRE NAT DE LA RECHERCHE SCIENTIFIQUE 1919, ROUTE DE MENDE MONTPELLIER, 34000 FRANCE				
8. PERFORMING ORGANIZATION REPORT NUMBER N/A				
9. SPONSORING/MONITORING AGENCY NAME(S) AND ADDRESS(ES) EOARD Unit 4515 APO AE 09421-4515				
10. SPONSOR/MONITOR'S ACRONYM(S) AFRL/AFOSR/IOE (EOARD)				
11. SPONSOR/MONITOR'S REPORT NUMBER(S) AFRL-AFOSR-UK-TR-2015-0035				
12. DISTRIBUTION/AVAILABILITY STATEMENT Distribution A: Approved for public release; distribution is unlimited.				
13. SUPPLEMENTARY NOTES COPYRIGHT MATERIAL WITH GOVERNMENT PURPOSE RIGHTS COPYRIGHT © 2014 Elsevier Ltd, 0008-6223				
14. ABSTRACT The objectives of this project were to identify the processes responsible for growth termination, creation and healing of defects, and chiral selectivity of single-walled carbon nanotubes, in order to develop strategies to increase nanotube length, improve the structural quality of samples, and improve the metallic semiconducting ratio of samples. Using in situ Raman measurements and scanning electron microscopy, we showed that reaction of the catalyst with support to form more refractory compounds can increase growth selectivity, showed that catalyst ripening, nanotube nucleation, and catalyst encapsulation can affect diameter and chirality, and showed that exposure to oxygen may be causing defects in growth.				
15. SUBJECT TERMS EOARD, carbon nanotubes, chiral selectivity				
16. SECURITY CLASSIFICATION OF: a. REPORT UNCLAS		17. LIMITATION OF ABSTRACT SAR	18. NUMBER OF PAGES 42	19a. NAME OF RESPONSIBLE PERSON PUTZ, VICTOR
				19b. TELEPHONE NUMBER (Include area code) 011-44-1895616013

## **FINAL TECHNICAL REPORT**

### **Grant FA8655-12-1-2059**

**Title:** Investigating the catalytic growth of carbon nanotubes with *in situ* Raman monitoring

**Duration (in months):** 36 (from 2012-04-01 to 2015-03-31)

**Principal Investigator:** Dr Vincent Jourdain, Associate Professor, Université de Montpellier

**Affiliation:** Laboratoire Charles Coulomb, UMR 5221 CNRS-Université de Montpellier

**Contact details:** Laboratoire Charles Coulomb, Place Bataillon, 34095 Montpellier Cedex 5, France. E-mail: [vincent.jourdain@univ-montp2.fr](mailto:vincent.jourdain@univ-montp2.fr). Tel.: +33 (0)4 67 14 47 78

**Associated investigator:** Benji Maruyama (AFRL/RXBN)

### **Context and objectives of the project (reminder)**

Single-walled carbon nanotubes (SWCNTs) constitute a family of tubular molecules having diameters in the nanometer range and made solely of carbon [1]. SWCNTs have received tremendous attention since their discovery due to the combination of exceptional electrical, thermal and mechanical properties. SWCNTs can be either metallic or semiconducting depending on their structure (also called chirality), they display electrical and thermal conductivities an order of magnitude higher than copper and they are both very light and extremely strong. SWCNTs are commonly produced by Catalytic Chemical Vapor Deposition (CCVD) using metal nanoparticles that catalyze the decomposition of a gaseous carbon source. The industrial development of nanotube-based technologies is presently hindered by several synthesis-related issues. First, the SWCNT length and the production yield are limited by the progressive deactivation of the catalyst particles during the CCVD process. Second, SWCNTs produced by CCVD usually display a lower structural quality and a higher amount of defective carbonaceous impurities. Third, as-grown SWCNT samples are mixtures of nanotubes of different chiralities and, therefore, different electrical properties.

The objectives of the project are to identify the chemical processes responsible for these issues and to develop new growth strategies to limit or control them.

- Aim 1: identify the processes responsible for the **growth termination** and devise strategies to increase the nanotube length,
- Aim 2: identify the processes responsible for the **creation and healing of defects** and devise strategies to improve the structural quality of SWCNT samples,
- Aim 3: identify the processes responsible for the **chiral selectivity** and devise strategies to improve the metallic/semiconducting ratio of SWCNT samples.

To address these goals, we propose to investigate the formation mechanism of SWCNTs using *in situ* Raman measurements in our recently built setup.

In addition to the original proposal, we proposed to investigate the formation mechanism of SWCNTs using *in situ* Scanning Electron Microscopy in environmental mode at high temperature (cf. email exchange with Program Officer Randall Pollak on 2014-01-30).

## Results (abstract)

Our first study [1] was devoted to elucidate the interplay of catalyst thickness and growth conditions in the activation and selectivity of single-walled carbon nanotube growth using cobalt deposited on Si/SiO<sub>2</sub> as a model system. *In situ* Raman studies revealed that thin catalyst layers require a higher pressure of carbon precursor to initiate nanotube growth. However, if the catalysts are pre-reduced, all catalyst thicknesses display the same low threshold pressure and a higher yield of single-walled carbon nanotubes. To explain these results, catalysts formed from a gradient of cobalt thickness were studied. Surface analyses showed that during the catalyst preparation, catalyst atoms at the interface with silica form small and hard-to-reduce silicate nanoparticles while the catalyst in excess leads to the formation of large oxide particles. Weakly-reducing conditions of pretreatment or synthesis are sufficient to reduce the large oxide particles and to lead to the growth of large-diameter multi-walled carbon nanostructures. However, highly-reducing conditions are required to reduce the small silicate domains into small cobalt particles able to grow single-walled carbon nanotubes. These results show that reaction of the catalyst with the support to form more refractory compounds greatly impact the nucleation yield and the growth selectivity of single-walled carbon nanotubes.

Our second study [2] was devoted to understand the chiral and diameter selectivity of model catalyst systems such as Ni/SiO<sub>2</sub> and Co/SiO<sub>2</sub>. As previously, our approach was based on systematic *in situ* and *ex situ* Raman investigations combined with post-growth analyses by HRTEM. We studied the evolution of the diameter and chirality distribution of SWCNTs with the synthesis time using two different approaches: i) truly *in situ* Raman monitoring and ii) *ex situ* Raman characterization of samples frozen at different times. In most cases, the diameter distribution of SWCNTs was observed to significantly evolve with time. The type of evolution (e.g. toward smaller or larger diameters) strongly depends on the growth conditions and we were able to map the different behaviors as a function of the growth domains. Post-growth analyses by HRTEM were performed to determine the underlying processes. Three size-dependent processes were found to affect the diameter distribution: catalyst ripening, nanotube nucleation and catalyst encapsulation. Beside the evolution of diameter which is the most noticeable process, we also studied how the evolution of the Raman spectra inform on the evolution of the chirality distribution during CCVD.

Our third study was initially devoted to address the same questions as the second one but at the individual nanotube level in order to suppress the averaging effect of ensemble measurements and to obtain the direct relationship between kinetic selectivity and nanotube chirality. Very few techniques are able to image individual CNTs in the conditions required for their growth (high temperature under an atmosphere of carbon precursor). High-Temperature Environmental Scanning Electron Microscopy (HT-ESEM) is potentially one of them. We were able to grow aligned SWCNTs (using monocrystal quartz substrate to align the tubes during their growth) in the HT-ESEM but the SWCNT growth in the HT-ESEM appeared to be too rapidly deactivated (<1s) to allow one to measure its kinetics despite our numerous attempts at finding more appropriate conditions. The main difference with standard CCVD growth being the low pressure, we suspected that oxygen traces may be at the origin of the ultrafast deactivation of SWCNT growth in the HT-ESEM. To investigate this, we performed a detailed study of subjecting SWCNTs to controlled amounts of oxygen at high temperature in the HT-ESEM chamber. We observed that exposure to oxygen at temperatures above 450°C induces defects along the nanotube walls causing the progressive cutting of nanotubes in many disconnected segments. We also evidenced that the oxidation of semiconducting SWCNTs is amplified by surface-trapped charges and e-beam exposure. We were thus able to provide a

detailed mechanism of the oxidation of SWCNTs on substrates. This work is submitted for publication [3].

These three studies are detailed in the annexes of this report.

## Perspectives

Understand the origin of the chiral selectivity of SWCNT growth and devise strategies to improve it are still topics of critical importance for the applications of SWCNTs in the future. The most sensible approach should rely on studies at the level of individual nanotubes to directly probe the chiral selectivity - nanotube structure relationship. Despite many advantages, *in situ* HT-ESEM is probably not the most appropriate method because it is extremely difficult to suppress gaseous contaminant traces in the HT-ESEM chamber. This is the reason why we are now developing another approach in order to image nanotube growth in normal CCVD growth conditions under atmospheric pressure. This approach is based on a novel concept of optical imaging of nanotubes on substrate initially developed by the Feng Wang group at Berkeley and relying on an intense, directional white light source (supercontinuum) and a polarization-enhanced contrast. In addition, this method also allows one to quickly determine the structure of each nanotube based on its absorption spectrum. By combining this method with our previous know-how of *in situ* studies by optical means, we wish to directly image individual SWCNTs during their growth and to correlate their growth kinetics with their individual structure.

## List of publications

- [1] ¨Interplay of interfacial compounds, catalyst thickness and carbon precursor supply in the selectivity of single-walled carbon nanotube growth, H. Navas, B. Maruyama, K. Weaver, M. Paillet, A. Zahab, F. Fossard, A. Loiseau, E. Quesnel, E. Anglaret, V. Jourdain, *Carbon* (2014), 80, 5996609.
- [2] ¨Evolution of the diameter and chirality distribution of single-walled carbon nanotubes during catalytic chemical vapor deposition, Hugo Navas, Vincent Jourdain, Thierry Michel, Matthieu Picher, Eric Anglaret, Annick Loiseau, Frédéric Fossard, Etienne Quesnel, manuscript in preparation.
- [3] ¨Oxidation Mechanism of Individual Single-Walled Carbon Nanotubes on Substrate Monitored by *in situ* Scanning Electron Microscopy, Hasan-al Mehedi, Johann Ravaux, Khadija Yazda, Thierry Michel, Saïd Tahir, Michaël Odorico, Renaud Podor, Vincent Jourdain, submitted for publication.

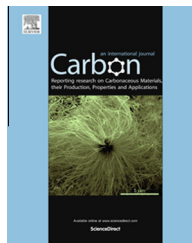
## ANNEXES



ELSEVIER

Available at [www.sciencedirect.com](http://www.sciencedirect.com)

ScienceDirect

journal homepage: [www.elsevier.com/locate/carbon](http://www.elsevier.com/locate/carbon)

# Interplay of interfacial compounds, catalyst thickness and carbon precursor supply in the selectivity of single-walled carbon nanotube growth

Hugo Navas <sup>a,b</sup>, Benji Maruyama <sup>c</sup>, Kent Weaver <sup>c</sup>, Matthieu Paillet <sup>a,b</sup>, Ahmed-Azmi Zahab <sup>a,b</sup>, Frédéric Fossard <sup>d</sup>, Annick Loiseau <sup>d</sup>, Etienne Quesnel <sup>e</sup>, Eric Anglaret <sup>a,b</sup>, Vincent Jourdain <sup>a,b,\*</sup>

<sup>a</sup> Université Montpellier 2, Laboratoire Charles Coulomb UMR 5221, F-34095 Montpellier, France

<sup>b</sup> CNRS, Laboratoire Charles Coulomb UMR 5221, F-34095 Montpellier, France

<sup>c</sup> US Air Force Research Laboratory, Materials & Manufacturing Directorate, RXAS, WPAFB, OH 45387, USA

<sup>d</sup> Laboratoire d'Études des Microstructures, ONERA-CNRS, F-92322 Châtillon, France

<sup>e</sup> CEA, Liten, DTNM, 17 rue des martyrs, 38054 Grenoble cedex 9, France

## ARTICLE INFO

### Article history:

Received 25 March 2014

Accepted 2 September 2014

Available online 15 September 2014

## ABSTRACT

This study is devoted to elucidate the interplay of catalyst thickness and growth conditions in the activation and selectivity of single-walled carbon nanotube growth using cobalt deposited on Si/SiO<sub>2</sub> as a model system. *In situ* Raman studies reveal that thin catalyst layers require a higher pressure of carbon precursor to initiate nanotube growth. However, if the catalysts are pre-reduced, all catalyst thicknesses display the same low threshold pressure and a higher yield of single-walled carbon nanotubes. To explain these results, catalysts formed from a gradient of cobalt thickness are studied. Surface analyses show that during the catalyst preparation, catalyst atoms at the interface with silica form small and hard-to-reduce silicate nanoparticles while the catalyst in excess leads to the formation of large oxide particles. Weakly-reducing conditions of pretreatment or synthesis are sufficient to reduce the large oxide particles and to lead to the growth of large-diameter multi-walled carbon nanostructures. However, highly-reducing conditions are required to reduce the small silicate domains into small cobalt particles able to grow single-walled carbon nanotubes. These results show that reaction of the catalyst with the support to form more refractory compounds greatly impact the nucleation yield and the growth selectivity of single-walled carbon nanotubes.

© 2014 Elsevier Ltd. All rights reserved.

## 1. Introduction

The applications of single-walled carbon nanotubes (SWCNTs) are hindered by the difficulty of selectively producing

SWCNTs free of other undesired carbonaceous materials (e.g. multi-walled carbon nanotubes, amorphous carbon). Catalytic chemical vapor deposition (CCVD), now the major method of SWCNT synthesis, involves the decomposition of

\* Corresponding author at: Université Montpellier 2, Laboratoire Charles Coulomb UMR 5221, F-34095 Montpellier, France.

E-mail address: [vincent.jourdain@um2.fr](mailto:vincent.jourdain@um2.fr) (V. Jourdain).

<http://dx.doi.org/10.1016/j.carbon.2014.09.003>

0008-6223/© 2014 Elsevier Ltd. All rights reserved.

a gaseous carbon precursor on catalyst nanoparticles acting both as nucleation centers and nanometric templates for the grown nanostructures [1–3]. In CCVD, it is commonly accepted that the size of the catalyst particle strongly dictates the nanotube diameter by limiting its lateral dimensions [4,5]. Controlling the size distribution of catalyst particles is therefore an essential aspect for the growth of SWCNTs with high selectivity, and has been the subject of numerous studies [6–8]. Among those, an elegant approach pioneered by the Noda group in Tokyo relies on the study of samples presenting a gradient of catalyst thickness [9–11]. This combinatorial method allows one to study a range of catalyst thicknesses in a single experimental run. Using this approach, the Noda group notably identified the optimal window of catalyst thickness for growing SWCNTs with high selectivity for various catalyst systems.

However, it is well-documented that for a given catalyst the selectivity of CNT growth is also strongly influenced by the growth conditions [4,12,13]. For instance, Lu et al. showed that using catalyst particles presenting a broad distribution of sizes, the diameter distribution of CNTs was upshifted when increasing the carbon feeding rate [12]. To explain this behavior, these authors hypothesized that small catalyst particles were poisoned by an excessive carbon supply while larger catalysts had too little carbon. In line with these results, Cheung et al. [4] reported that when using catalyst particles of different sizes (3, 9 and 13 nm), small particles required a lower carbon supply rate than large ones. More recently, some of us reported that there was actually an optimal pressure of carbon precursor for growing small-diameter SWCNTs [14]: below and above this optimal pressure, the nanotube distribution is shifted toward larger diameters. By performing two consecutive growths at different carbon supplies, we showed that at too high of a carbon supply small particles were more rapidly encapsulated than large ones. At too low carbon supply, the lack of small-diameter SWCNTs was found to originate from impeded nanotube nucleation from the smallest catalyst particles. However, the physical explanation of this phenomenon remained unresolved at the time.

Here, to elucidate the interplay of the catalyst size and the carbon supply in the selectivity of carbon nanotube growth, we subjected samples having different thicknesses of metal catalyst or a gradient of catalyst thickness to various pretreatment and synthesis atmospheres. The growth experiments were monitored *in situ* by Raman spectroscopy to identify for each catalyst thickness the threshold gas conditions for nanotube nucleation. The post-growth samples were further characterized by Raman mapping, high-resolution transmission electron microscopy (HRTEM) and X-ray photoelectron spectroscopy along the catalyst gradient. Our study demonstrates that thin catalyst layers (typically less than 10 Å) require a higher pressure of carbon precursor for nucleating and growing carbon nanotubes. XPS analyses show that this behavior is caused by the lower reducibility of small catalyst particles forming mixed compounds at the interface with the silica support. Our study explains why an appropriate combination of catalyst thickness and reducing conditions is required to selectively grow SWCNTs without contamination from other multi-walled and disordered carbon nanostructures.

## 2. Experimental

10-nm layers of  $\text{SiO}_2$  were deposited by ion beam sputtering (IBS) onto Si substrates, followed by a cobalt layer of constant thickness (0.3 nm, 1 nm and 2 nm) measured with a quartz balance. Samples with cobalt thickness gradients were also prepared by sputtering a 30 Å-thick layer of cobalt through a deposition mask. For each sample, the catalyst thickness along the gradient was measured by Electron Probe Micro Analysis (EPMA). The measurement accuracy is  $\pm 10\%$  of the thickness which corresponds to the accuracy of the quartz thickness monitor used for measuring the calibration thickness. All samples were calcined in air at 700 °C before synthesis to remove carbon contaminants. This oxidative pre-treatment leads to a significant roughening of the catalyst surface with the formation of particles of up to 10–20 nm for certain catalyst thicknesses (see AFM data in [Fig. S1 of the Supplementary information file](#)). CCVD growths were performed in a cold-wall micro-reactor (Linkam TS1500) allowing *in situ* Raman measurements. *In situ* micro-Raman measurements at 647 nm (1.92 eV) were recorded with a Horiba Jobin Yvon T64000 equipped with a microscope (50 $\times$  objective, laser spot of ca. 2  $\mu\text{m}$ ). At this laser excitation, *in situ* Raman measurements are not impeded by the black-body radiation if the temperature is less than 800–850 °C.

Acetylene or ethanol was used as carbon precursor. Ethanol vapor was supplied by bubbling argon (Air Liquid 99.999%) through a flask of liquid ethanol (Fluka, 99.8%) thermostated at 0 °C. Acetylene was supplied from a gas cylinder of argon mixed with acetylene at 1000 ppm (Air Liquid). An additional argon line was used to dilute the gas mixture and adjust the final precursor partial pressure. The total gas flow was 1422 sccm.

Post-growth characterization was performed by Raman spectroscopy, HR-TEM, XPS, and scanning electron microscopy (SEM). Raman mapping was performed at a laser wavelength of 532 nm (2.33 eV) using an M-686 XY stage (PI) and an Acton SP2500 spectrometer (Princeton Instruments). The diameter of the laser spot was ca. 1  $\mu\text{m}$ . TEM samples were prepared by scratching the surface of the samples with a diamond tip and contacting them with TEM grids (holey carbon films, Agar). This preparation method not only allowed characterizing the carbon structures but also the catalyst particles attached to thin  $\text{SiO}_2$  support fragments. HR-TEM and Scanning TEM High Angle Annular Dark Field (STEM HAADF) images were taken using two field emission TEMs: a ZEISS Libra 200 MC and a FEI CM20, working at 200 kV. XPS characterization were performed with an ESCALAB 250 from Thermo Electron with an Al K $\alpha$  excitation source (1486.6 eV) and a spot diameter of ca. 400  $\mu\text{m}$ . Samples were characterized by XPS right after CVD to minimize air exposure (less than 15 min). XPS spectra were calibrated in energy with respect to the C 1s component at 284.8 eV or the Si 2p peak of  $\text{SiO}_2$  at 103.4 eV. SEM pictures were acquired with a Hitachi S4800.

## 3. Results and discussion

We first studied the influence of the carbon precursor pressure on the initiation of nanotube growth using *in situ* Raman

measurements. We previously reported that a threshold precursor pressure exists under which no nanotube growth can be observed even after 30–60 min of exposure to the carbon feedstock [15]. Above this threshold pressure, nanotubes start growing at a fast rate [16]. Here, we used samples with different nominal thicknesses of cobalt (3, 10 and 20 Å) to determine whether this threshold pressure of nucleation was dependent on the catalyst thickness. Fig. 1a–c display the evolution of the G-band integrated intensity during the step-by-step increase of the precursor concentration (acetylene). Once the precursor concentration reached a threshold value we observed that the G band characteristic of  $sp^2$  carbon materials appeared and rapidly grew. To check the validity of these threshold pressure measurements, we performed three control experiments: (i) we checked that the incubation time at constant acetylene concentration is significantly less than the time interval chosen during each step (see Fig. S2a and b), (ii) we checked that the chosen rates of acetylene addition were sufficient slow not to impact the measured value of the threshold pressure (see Fig. S2c), (iii) we checked that no growth is observed even after 1000 s if an acetylene concentration lower than the threshold value is applied. This confirms that the growth initiation is primarily the consequence of the precursor pressure value and is little affected by the incubation time which appears negligible (20–50 s) in the experimental conditions used herein. In addition, the abruptness of the growth initiation is indicative of a thermodynamic transition of the system (by opposition to a

simple increase of chemical kinetics). Three processes can be hypothesized to account for this sharp transition: (i) the reduction of the catalyst particles, (ii) the precipitation of carbon nuclei at the catalyst surface and (iii) the lift-off of the carbon cap (which is predicted to be dependent on the chemical potential of carbon atoms inside the particle [17]). Most importantly, the threshold concentration is found quite similar for the 10 Å and 20 Å cobalt thickness (16 ppm of  $C_2H_2$ ) while it is more than twice higher for a thickness of 3 Å (40 ppm of  $C_2H_2$ ).

Notable differences can also be observed in the post-growth Raman spectra (Fig. 1d and e). The Raman spectrum of the 3 Å sample displays the characteristic features of small-diameter SWCNTs (i.e. typically less than 2 nm): a narrow and intense G band with marked G<sup>−</sup> shoulder peaks at 1540–1560  $cm^{-1}$ , intense radial breathing modes (RBM), a high ratio of the integrated intensity of the G band to the D band (G/D), and a D band significantly downshifted compared to the reference position of graphene at this laser wavelength [18] (see the vertical dashed line in Fig. 1d). For the larger thicknesses samples (10 Å and 20 Å), the relative intensity of small-diameter CNT features decreases: (i) the G band displays an additional broad contribution at around 1580  $cm^{-1}$  which progressively hides the G<sup>−</sup> shoulder peaks and broadens the main G peak, (ii) the G/D ratio decreases, and (iii) the D band displays additional contributions at frequencies close to or higher than the reference position of monolayer graphene (i.e. without curvature or stacking effects). All these

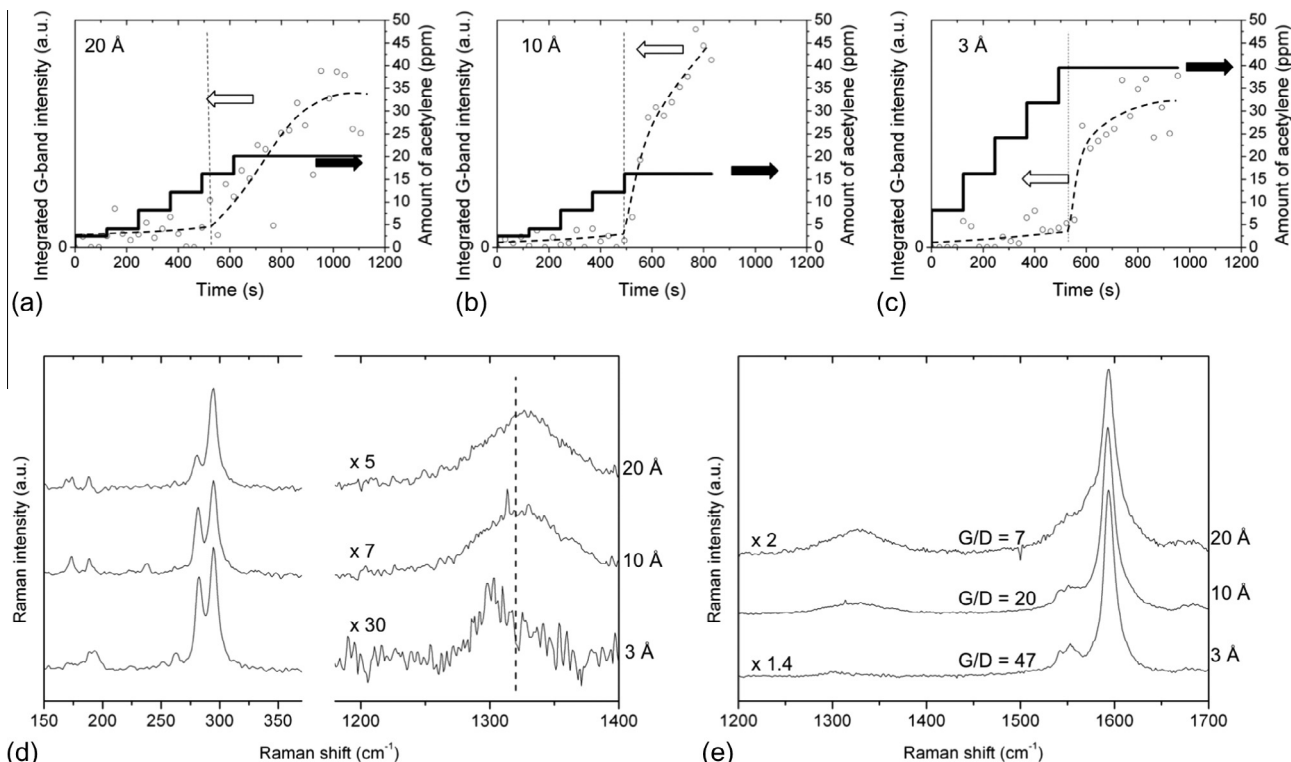


Fig. 1 – (a–c) Evolution of the integrated G-band intensity (open circles) with increasing partial pressure of acetylene (solid line) for different thicknesses of cobalt (synthesis temperature 725 °C). The dotted vertical line indicates the onset of nanotube growth. (d,e) Corresponding post-growth Raman spectra in the frequency range of the RBMs, D band and G band. In Fig. 1d, the vertical dashed line indicates the reference position of the D-band of graphene at this laser wavelength (647 nm).

observations are consistent with an increasing amount of low-curvature and multi-walled disordered carbon structures. Taking into account that the Raman scattering of small-diameter CNTs is enhanced by several orders of magnitude due to the resonance Raman effect [19], the Raman data suggest that low-curvature carbon structures constitute the majority product of the 10 and 20 Å samples. Noteworthy, the RBM profile (i.e. the relative intensities of the RBMs) is little affected by the change of catalyst thickness (between 3 and 20 Å). Only the relative proportion of SWCNTs and low-curvature carbon by-products appears to change between the three samples.

To confirm the Raman interpretation, HRTEM and STEM HAADF characterizations were performed. As shown in Fig. 2, the carbon structures grown with the 3 Å and 10 Å samples are considerably different. The 3 Å sample displays entangled single- and few-walled CNTs with diameters all less than 5 nm (Fig. 2a). In contrast, the 10 Å sample mostly displays multi-walled carbon nanostructures (both tubes and shells) with diameters between 7 and 20 nm (Fig. 2c). While the Raman spectra display strong features of SWCNTs, the TEM images displayed no or little evidence of them among the MWCNTs and substrate fragments. This observation is in line with our previous report [19] that for mixtures of SWCNTs and MWCNTs, the resonant effect in Raman spectroscopy generally leads to overestimating the proportion of SWCNTs while TEM leads to the opposite flaw.

Beside carbon nanotubes, the size distribution of catalyst particles can also be characterized by HR-TEM: the 3 Å sample presents a distribution of particles comprised between 1 and 6 nm (Fig. 2b) while the 10 Å sample displays a broader distribution of particle sizes comprised between 1 and 20 nm (Fig. 2d). Noteworthy, the small catalyst particles in the 10 Å sample exposed to 16 ppm of C<sub>2</sub>H<sub>2</sub> present a significantly lower contrast compared with the 3 Å sample that was exposed to 40 ppm of acetylene. For the 3 Å sample, the particle size distribution matches reasonably well with the nanotube diameter distribution, which suggests that particles of all sizes were active at the C<sub>2</sub>H<sub>2</sub> concentration of 40 ppm. In contrast, for the 10 Å sample grown at the threshold concentration of 16 ppm of C<sub>2</sub>H<sub>2</sub>, a significant mismatch is observed between the size distribution of catalyst particles and the diameter distribution of carbon nanotubes.

To explain these results, we submitted new catalyst samples to a reducing pretreatment under H<sub>2</sub> (5% H<sub>2</sub> in argon during 5 min at 725 °C) before performing the same threshold pressure experiments. As shown in Fig. 3a–c, all pre-reduced samples then displayed the same threshold concentration of 16 ppm of C<sub>2</sub>H<sub>2</sub> whatever the catalyst thickness. The 3 Å sample displayed a Raman spectrum quite similar to the experiment without reducing pretreatment but with slightly more SWCNTs of diameters in the 1–2 nm range (compare RBMs and G-peaks in Figs. 1 and 3d and e). In contrast, the Raman spectra of the 10 and 20 Å samples are considerably

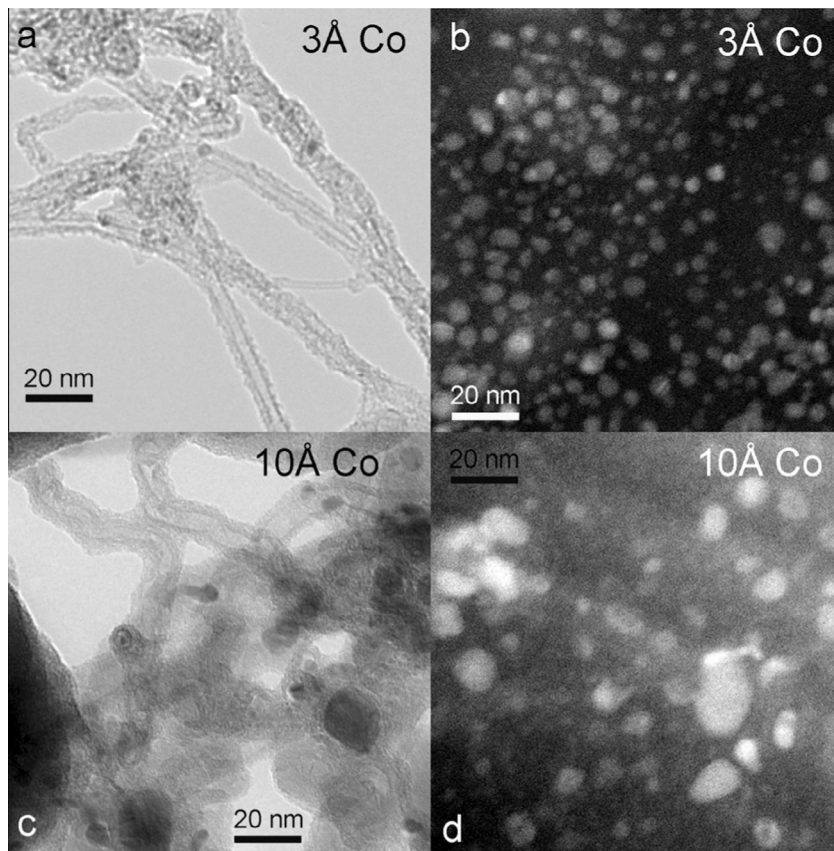


**Fig. 2 – Post-growth electron microscopy images of the samples with cobalt thicknesses of 3 Å and 10 Å (threshold precursor pressure). (a,c) HR-TEM images of the grown CNTs, (b,d) HAADF STEM images at the Co particles supported on the SiO<sub>2</sub> underlayer.**

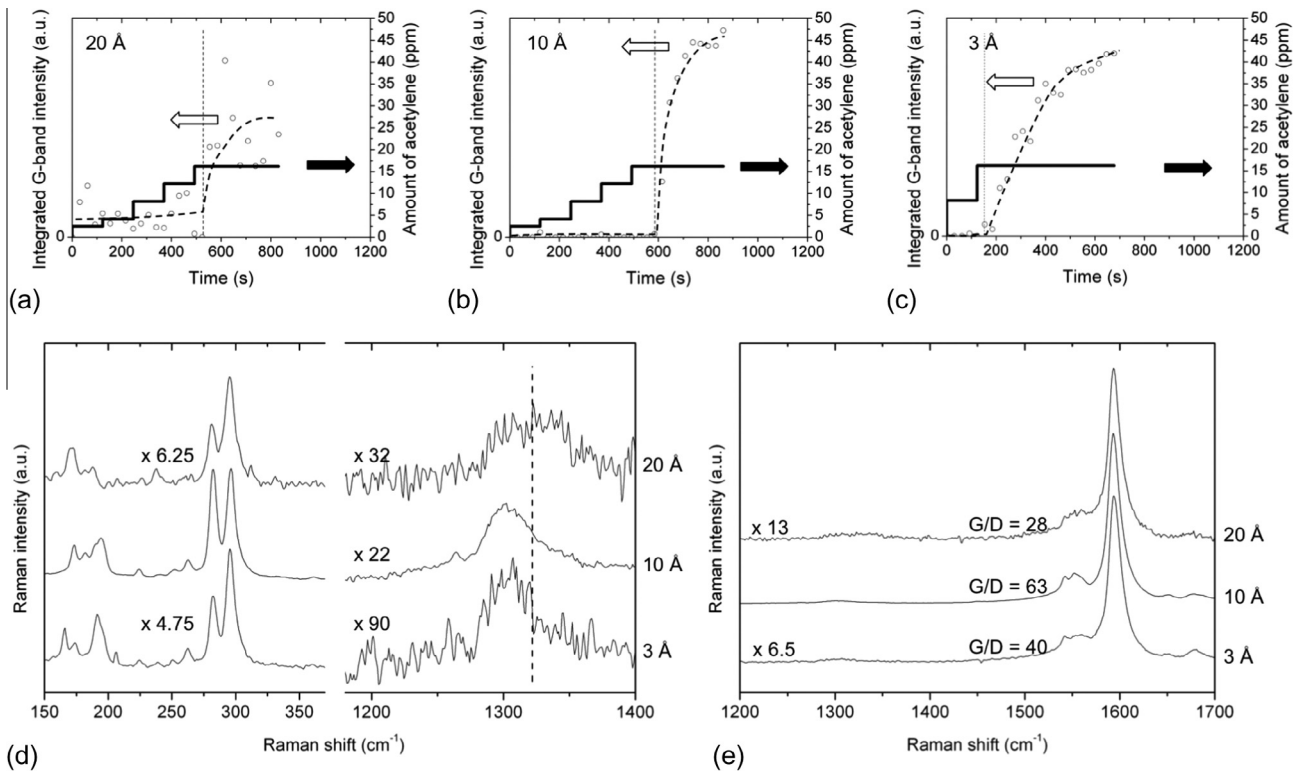


**Fig. 3 – Pre-reduced samples: (a–c)** Evolution of the integrated G-band intensity (open circles) while increasing the partial pressure of acetylene (black line) for different thicknesses of cobalt (synthesis temperature 725 °C). **(d,e)** Corresponding post-growth Raman spectra. The vertical dashed line indicates the reference position of the D-band of graphene at this laser wavelength (647 nm).

different from the experiment without reducing pretreatment: (i) the G band profile displays no additional contribution at 1580 cm<sup>-1</sup> and is comparable to the profile of the 3 Å sample, (ii) the G/D ratio is 3–4 times higher, and (iii) the D band is narrower and downshifted compared with the same sample without reducing pretreatment.

These samples were characterized by HR-TEM. Being grown at the very limit of the growth window, they display a low yield of CNTs compared to samples grown in optimal conditions. Short SWCNTs (isolated or in a bundle) extending out of the SiO<sub>2</sub> fragments are still clearly discernible and easily found (Fig. 4) while MWCNTs are quasi-absent. By contrast, for unreduced samples, it was extremely difficult to find SWCNTs by TEM even after hours of dedicated search while MWCNTs were commonly found (Fig. 2a and c). TEM observations therefore confirm a much higher yield of SWCNTs compared to MWCNTs if the samples are subjected to a reducing pretreatment. The size distribution of the catalyst particles did not appear extensively modified by the reducing pretreatment (see Figs. 4c,f and 2b,d). However, the small particles in the 10 Å sample display a TEM contrast noticeably enhanced compared with those of the same sample without reducing pretreatment. These observations suggest that the main effect of the reducing pre-treatment was to modify the chemical state of the catalyst particles rather than their size distribution.

To investigate the reducing effect of the carbon precursor itself in CVD conditions, we characterized the catalyst by

XPS at different steps of the synthesis process. As shown in Fig. 5, the Co 2p XPS spectrum of the as-deposited 10 Å-thick catalyst samples (thin black line in Fig. 5) presents 2p<sub>3/2</sub> and 2p<sub>1/2</sub> peaks at 781.1 eV and 797.0 eV, respectively, together with intense satellite structures. These features are compatible with both CoO (reference positions at 780.6 eV for 2p<sub>3/2</sub> and 796.8 eV for 2p<sub>1/2</sub> [20,21]) and cobalt silicates (reference positions at 781.5–782.5 eV for 2p<sub>3/2</sub> and around 798 eV for 2p<sub>1/2</sub> [22–24]) but not with cobalt silicides (reference position of 2p<sub>3/2</sub> at 778.5 eV [25]). After calcination under air at 700 °C (red dashed line), both peaks are shifted to lower binding energies (780.3 eV for 2p<sub>3/2</sub>, 795.8 eV for 2p<sub>1/2</sub>) and the satellite structures diminish in good agreement with a conversion of CoO into Co<sub>3</sub>O<sub>4</sub> [20]. The peak features are however broad which suggests a mixture of different cobalt compounds (CoO, Co<sub>3</sub>O<sub>4</sub> and possibly cobalt silicates). After exposure to acetylene during CVD (bold grey and black lines), CoO and Co<sub>3</sub>O<sub>4</sub> contributions essentially disappear and the Co 2p spectrum is dominated by the contribution of metallic cobalt (Co 2p<sub>3/2</sub> and 2p<sub>1/2</sub> at 778.3 and 793.3 eV, respectively [26]). Importantly, an additional peak becomes clearly distinguishable at 782.3 eV which is at too high energy for CoO and can only be attributed to cobalt silicates [22–24]. If the synthesis temperature is increased (e.g. 850 °C), the additional peak at 782.3 eV considerably drops down and more intense SWCNT features are observed in the Raman spectrum. Together these results support that small particles of cobalt silicate are formed during the catalyst deposition or, more likely, during

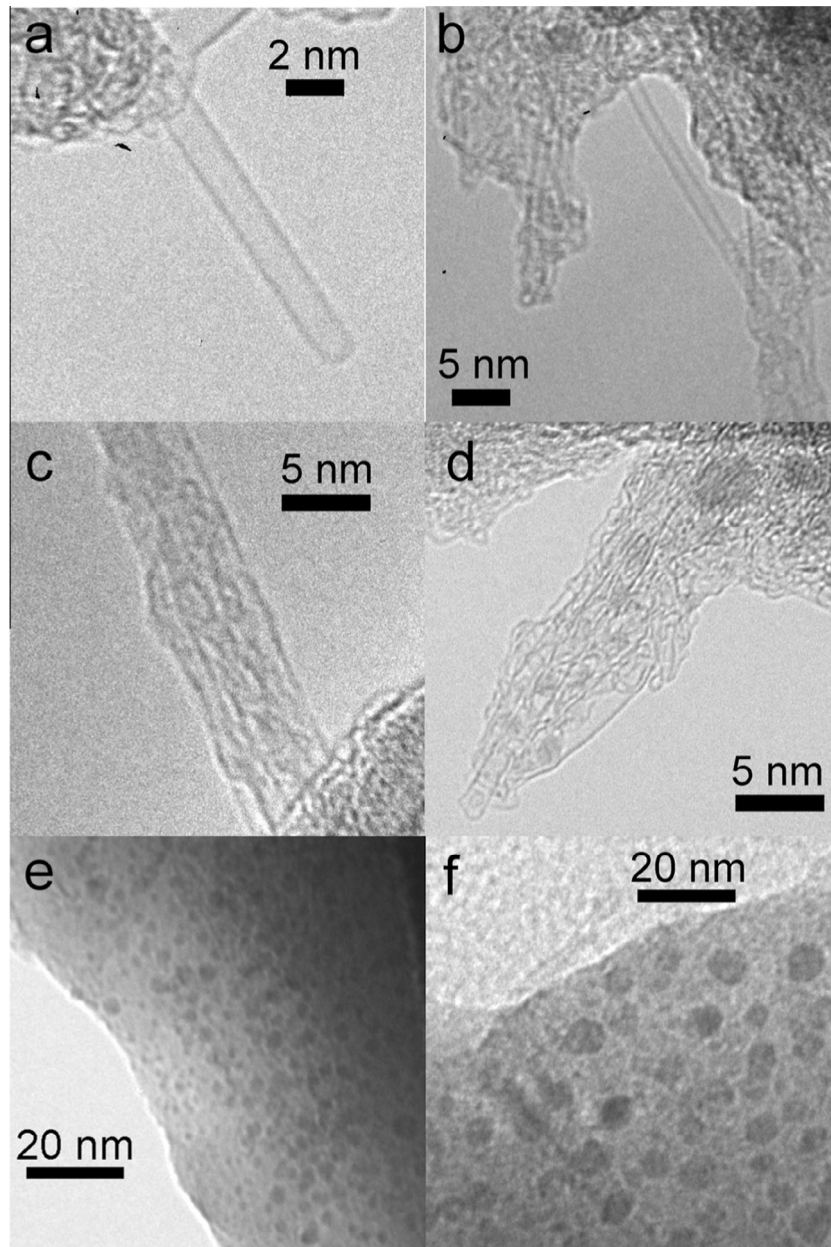


**Fig. 4 – Post-growth HR-TEM images of the samples subjected to a reducing pre-treatment: SWCNTs grown from Co thickness of 3 Å (a–c) and 10 Å (d), catalyst particles on  $\text{SiO}_2$  underlayer for the samples of Co thickness of 3 Å (e) and 10 Å (f).**

the calcination in air. The formation of cobalt silicates during the oxidative pretreatment is indeed a common observation for Co/SiO<sub>2</sub>-based catalysts such as Fischer-Tropsch catalysts [27,28]. However, if Co/SiO<sub>2</sub> is annealed under vacuum, Fouquet et al. [29] evidenced the formation of cobalt silicides instead of cobalt silicates. Our results also support that small cobalt silicate particles can be effective for the formation of small-diameter CNTs but require much higher temperatures than cobalt oxides to be reduced into metallic cobalt in agreement with previous reports from Pfefferle et al. [30,31]. If this interpretation of the influence of the temperature is correct, one would expect that a more reducing atmosphere (i.e. a higher acetylene concentration or a hydrogen pretreatment) is also needed to reduce small cobalt silicate particles and

make them active for the growth of SWCNTs. This hypothesis would notably explain the results of the threshold pressure experiments.

To address this question for a large range of catalyst thicknesses, we then moved to catalyst samples presenting a gradient of cobalt thickness. Fig. 6 shows the Raman data collected along the thickness gradient for three CNT samples prepared in different gas conditions using ethanol as carbon precursor: at high and low pressures of carbon precursor, and at low precursor pressure after a reducing pretreatment. At high precursor pressure (Fig. 6a and b), SWCNT features (G<sup>−</sup>, RBM, high G/D, downshifted D-band) are observed for all catalyst thicknesses and most markedly for Co thicknesses between 2 and 20 Å. As previously observed, the RBM profile

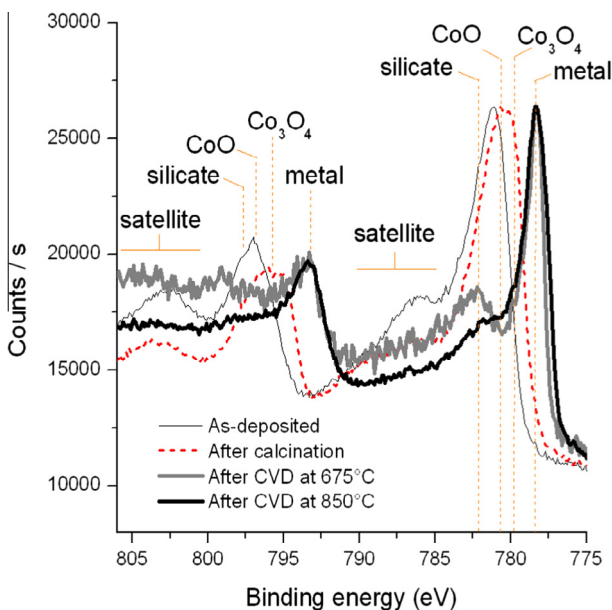


**Fig. 5 – XPS spectra of the Co 2p level of a 10 Å Co catalyst sample: after cobalt deposition (thin black line), after calcination (red dashed line), and after a CVD synthesis with 66 ppm C<sub>2</sub>H<sub>2</sub> at 675 °C and 850 °C (grey and black bold lines, respectively). (A colour version of this figure can be viewed online.)**

remains quite similar whatever the catalyst thickness. At high catalyst thickness (>10 Å), the progressive increase, broadening and upshift of the D band indicates a higher abundance of multi-walled and disordered carbon structures. This is correlated with the observation of large particles (tens of nm large) all over the surface in SEM pictures (see Fig. S3 in the Supplementary information file). If a lower precursor pressure is used (Fig. 6c and d), SWCNT features are dramatically reduced whatever the catalyst thickness. More precisely, for thicknesses lower than 10 Å, very weak signatures of SWCNTs can still be observed. However, for thicknesses higher than 10 Å, the Raman spectra display a G/D ratio close to 1 accompanied by a dramatic decrease of the signal of the silicon support, which are characteristic features of a thick and absorbing layer of disordered carbon structures. When the catalyst was subjected to a reducing pre-treatment the growth of SWCNTs was strongly promoted even at low precursor pressure (Fig. 6e and f): the RBM intensities for instance are increased by 1–2 orders of magnitude by comparison with the same synthesis without reducing pretreatment. However, the proportion of SWCNT is not as high as that directly obtained at high precursor pressures probably because catalyst coarsening is no more negligible at the time scale of nanotube growth. Generally speaking, the results obtained on thickness gradients allow generalizing the conclusion that small catalyst thicknesses require more reducing conditions through either a higher carbon precursor pressure or the addition of a reducing agent to become active for CNT growth. The question that follows is therefore that of the origin of this lower reducibility: silicate formation or size effect.

Beside this general trend, Fig. 6a,c and e display a more complex evolution of the G-band intensity as a function of the catalyst thickness marked by the presence of peaks and valleys. Sharp variations are notably observed close to the substrate edges (see double arrows in Fig. 6a,c and e). Since these features occur in regions of no or little variation of catalyst thickness, they are attributed to edge effects (i.e. local variations of the precursor supply/gas phase composition close to the substrate edges), a common phenomenon in CVD [32–34]. A striking example is the strong increase of intensity between points A and B in Fig. 6c and e which cannot be accounted by a thickness effect since the catalyst thickness is nearly constant between these two points. These edge effects provide an additional illustration of the interplay of catalyst thickness and (local) growth conditions on the efficiency of nanotube growth. Our observations show that edge effects are generally beneficial to the growth of SWCNTs (see peaks at positions “G” in Fig. 6a, “B” and “H” in Fig. 6e) and detrimental to the growth of MWCNTs (see valleys at positions “A” in Fig. 6a,c and e). In addition to these edge features, a profound valley marking the frontier between SWNT-like and MWCNT-like Raman features is observed for the two samples grown at low precursor pressures (see position “E” in Fig. 6e and position “D” in Fig. 6c). A growth valley separating SWCNT-rich region and MWCNT-rich region in catalyst gradient samples was previously reported by the Noda group [11] whose origin is discussed hereafter.

To complete this analysis, we performed XPS analyses at different positions along the catalyst gradient. Fig. 7a–c compare the Co 2p spectra obtained at three different catalyst thicknesses for the samples grown at low and high pressures of carbon precursor (black and red curves, respectively). The first observation is that, whatever the catalyst thickness, the proportion of oxidized forms of Co (oxides and silicates) is much lower for the sample exposed to a high pressure of carbon precursor. This confirms that at low precursor pressure a large fraction of catalyst particles is not reduced to metallic cobalt and explains why the carbon nanotube yield is so low in these conditions. For the sample grown at low precursor pressure (black curves in Fig. 7), it is difficult to resolve the contributions of oxides and silicates in the broad Co(II) peaks (between 780.5 eV and 783 eV for Co 2p<sub>3/2</sub> and between 796 eV and 799 eV for Co 2p<sub>1/2</sub>). However, when the precursor pressure is increased (red curves in Fig. 7), it is observed that the Co(II) peaks are systematically shifted to higher binding energies that can only be assigned to cobalt silicates. This confirms the presence of cobalt silicate particles requiring higher precursor pressures, longer times and higher temperatures than cobalt oxides to be converted into metallic cobalt. For the sample grown at high precursor pressure where the contribution of cobalt silicates is clearly resolved, a third observation is that the ratio of silicates to metallic cobalt is lowest for the highest thickness of cobalt. This supports that, for a sufficiently thick layer of cobalt, most of the cobalt does not interact with the SiO<sub>2</sub> support and therefore simply form cobalt oxide particles that are easily reduced to metallic Co.

Besides the general trend associated with the thickness variation, it is also observed that the catalyst is significantly more reduced close to the substrate edge (compare Fig. 7a

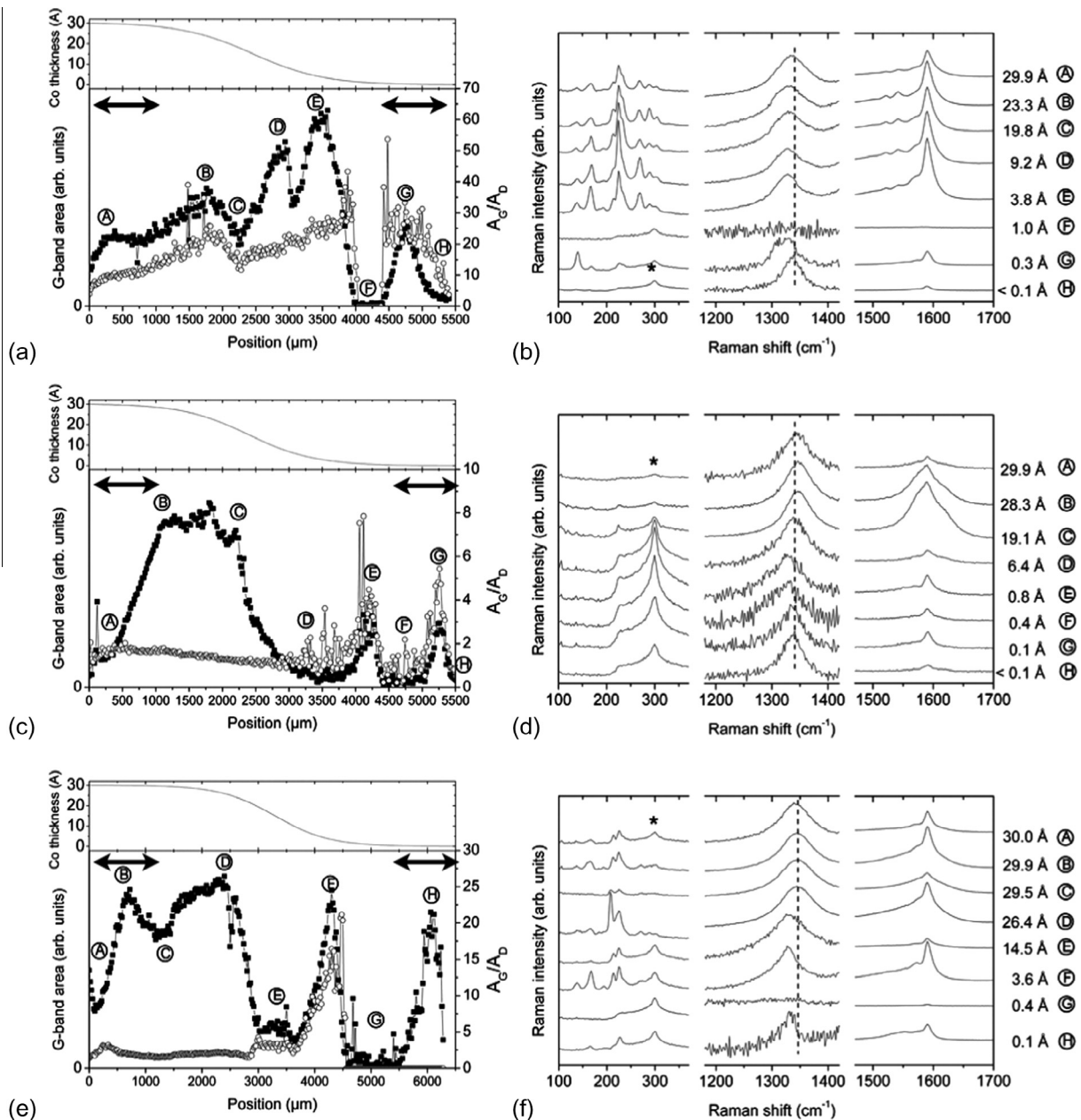


**Fig. 6** – Cobalt thickness (upper insert), G-band intensity (black squares), G/D ratio (open circles) and Raman spectra (right column) as a function of the position along the catalyst gradient sample for the samples synthesized at 640 Pa of ethanol (a,b), 80 Pa of ethanol (c,d) and 80 Pa of ethanol after a reducing pretreatment (e,f). All syntheses were performed at 750 °C. The laser wavelength was 532 nm (2.33 eV). The double arrows in Fig. 6a,c and e indicate the extent of the edge effects. The D-bands were normalized to facilitate the comparison of their profiles. The vertical dashed line represents the reference position of the D-band of graphene at 532 nm. For points with  $A_D$  close to zero, the  $A_G/A_D$  values were not plotted.

with b and c). This supports that the catalyst experiences more reducing conditions when approaching the edge of the substrate. This higher reduction rate coincides with sharp variations of the CNT yield observed by Raman mapping at the catalyst edge (see peaks at positions “G” in Fig. 6a and c). This correlation supports that more reducing conditions at the substrate edges are beneficial to the growth of SWCNTs when growth activation is limited by catalyst reduction.

To account for the experimental dependence of the CNT growth selectivity with the catalyst thickness, Noda et al. [11] proposed the existence of two different mechanisms of particle formation: (i) surface diffusion of cobalt adatoms prevailing at low cobalt thickness and leading to the formation of small particles (less than 5 nm) and (ii) surface dewetting prevailing for thick catalyst layers and leading to large particles (10–30 nm). Although this proposition provided a first explanation for the SWCNT vs. MWCNT selectivity, the

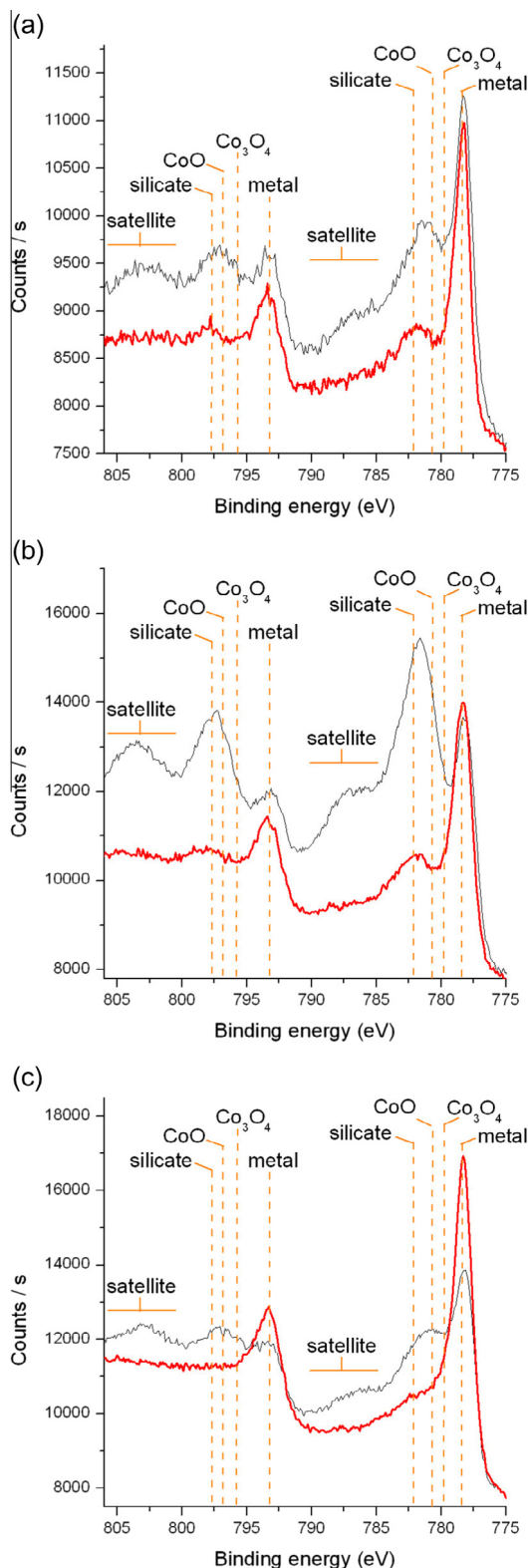


**Fig. 7 – Co 2p XPS spectra for at different positions along the thickness gradient of cobalt for the samples grown at 80 Pa (black line) and 640 Pa (broad red line) of ethanol without reducing pretreatment: (a)  $e_{\text{Co}} \sim 0.4\text{--}1.2 \text{ \AA}$  (close to the low-thickness edge), (b)  $e_{\text{Co}} = 2\text{--}5 \text{ \AA}$ , (c)  $24\text{--}27 \text{ \AA}$ . (A colour version of this figure can be viewed online.)**

rational behind the existence of two different mechanisms was lacking at that time. Our study allows rationalizing and generalizing this picture by taking into account the crucial role of interfacial compounds and of the reducing conditions on the activation and selectivity of CNT growth.

Fig. 8 schematically illustrates the general picture arising from our studies. Following catalyst deposition and exposure to air (step 1 in Fig. 8), the catalyst essentially consists of mixed Co(II) cobalt compounds. The oxidative heat treatment (step 2 in Fig. 8) leads to the formation of small particles of cobalt silicate at the Co/SiO<sub>2</sub> interface while the cobalt in excess leads to large particles (5–20 nm, see AFM data in Fig. S1) with a higher degree of oxidation (i.e. Co<sub>3</sub>O<sub>4</sub>) by surface dewetting. Under weakly-reducing growth conditions (i.e. at low temperature or at low precursor pressure), XPS analysis shows that the large oxide particles are efficiently reduced to metallic cobalt but also reveal the persistence of hard-to-reduce cobalt silicate particles (case 2b in Fig. 8). This accounts for the bimodal size distribution commonly observed for Co/SiO<sub>2</sub> catalysts [35]. In such weakly-reducing growth conditions, active catalyst particles are essentially large ones which lead to the growth of large-diameter multi-walled carbon structures and to very few SWCNTs.

In contrast, if highly-reducing growth conditions are used (case 2a in Fig. 8), small cobalt silicate domains can be reduced to small cobalt particles, thus leading to a huge increase of the formation of SWCNTs. The proportion of SWCNTs is largest where the catalyst thickness was low enough to minimize the formation of large cobalt oxide particles. Beside the experiments on gradient samples, this difference of reducibility also accounts for the higher threshold of precursor pressure required for activating nanotube growth from thin catalyst layers observed in Fig. 1.

Alternatively, a reducing pretreatment (step 3 in Fig. 8) can be applied in order to reduce the small cobalt silicate particles into metallic cobalt before introducing the carbon source. The growth of a high proportion of SWCNTs is then made possible even in weakly-reducing growth conditions (case 3b in Fig. 8). However, the SWCNT yield is lower than when simply using a high precursor pressure (case 2a) and a large valley separating SWCNT and MWCNT appears, as also reported by Noda et al. [11]. We propose that both features originate from the progressive disappearance of the smallest catalyst particles (by Smoluchowski ripening, i.e. migration–coalescence, [36] or Ostwald ripening [37]) once reduced and when exposed to low precursor pressure synthesis conditions. For pre-reduced catalyst particles exposed to a sufficiently low pressure of carbon precursor, catalyst ripening is expected to proceed faster than SWCNT nucleation, therefore decreasing the SWCNT yield [37–39]. At low catalyst thickness (i.e. low surface density), many particles remain sufficiently small to produce SWCNTs giving rise to an intense Raman signal due to the resonance effect. At high catalyst thickness, very large metal particles are produced leading to the growth of large amounts of multi-walled carbon structures (see SEM images in Fig. S4). At intermediate catalyst thickness, catalyst ripening essentially leads to particles which are too large for SWCNT growth but in too small amounts to produce multi-walled carbon

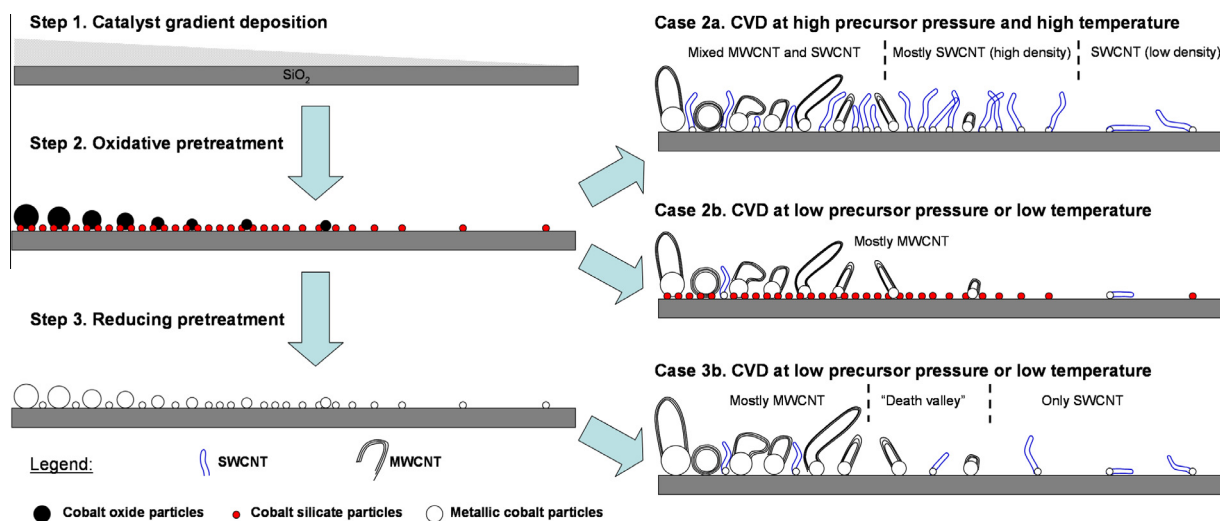


**Fig. 8 – Schematic model of the interplay of catalyst thickness and growth conditions on the selectivity of CNT growth. (A colour version of this figure can be viewed online.)**

nanostructures giving an appreciable Raman signal. This causes an apparent valley in the Raman map of the gradient samples subjected to a low precursor pressure.

Beside the influence of the catalyst thickness, the CNT yield is influenced by edge effects. These edge effects appear as an additional illustration of the interplay of catalyst thickness and precursor pressure in the selective activation of CNT growth. Catalyst atoms close to the substrate edges are subjected to higher precursor partial pressures and reducing conditions. These conditions promote the growth of SWCNTs since its activation is limited by silicate reduction. Edge conditions are also detrimental to the growth of MWCNT at high catalyst thickness (see Fig. 6c and e). This appears related to the formation of very large particles ( $>40$ – $50$  nm) which become encapsulated by a thick carbon layer instead of yielding CNTs (see SEM pictures in Figs. S3 and S4).

#### 4. Conclusion

This work shows that the observed interplay of catalyst size and growth conditions in the activation of CNT growth is primarily a consequence of the formation of interfacial compounds of low reducibility. The catalyst thickness influences the relative proportions between interfacial compounds formed with the silica support and large cobalt oxide particles formed by surface dewetting. These bimodal size and chemical distributions strongly impact the conditions required for activating nanotube growth: weakly-reducing conditions are sufficient to activate large oxide particles while highly-reducing conditions are required for reducing the more stable silicate particles. For thin catalyst layers (i.e. of nominal thickness typically less than  $5$  Å), this effect causes a significant increase of the threshold precursor pressure and temperature required for initiating SWCNT growth. However, catalyst particles are more subject to ripening once reduced. It follows that the highest nanotube yields are obtained with no reducing pretreatment but by directly using the carbon source to reduce the catalyst particles and feed them with carbon. An important question is whether the behavior brought to light

in this work is specific of the Co/SiO<sub>2</sub> couple or generic to a large class of catalyst systems used for CNT growth. Electropositive metals such as iron and cobalt deposited on silica and alumina are known to easily form mixed compounds and would be expected to display similar behaviors. However, less electropositive metals such as nickel and copper do not have such a strong tendency and the mixed compounds thus formed are less stable. It would be interesting to compare the behaviors of such catalyst systems with the one evidenced in this work.

#### Acknowledgements

Support from ANR (Project SOS Nanotube ANR-09-NANO-028), AFOSR and EOARD (contract FA8655-12-1-2059) is gratefully acknowledged. The authors thank Valérie Flaud, Bertrand Rebière, Viviane Muffato and Saïd Tahir for technical support.

#### Appendix A. Supplementary data

Supplementary data associated with this article can be found, in the online version, at <http://dx.doi.org/10.1016/j.carbon.2014.09.003>.

#### REFERENCES

- [1] Dai H, Rinzler AG, Nikolaev P, Thess A, Colbert DT, Smalley RE. Single-wall nanotubes produced by metal-catalyzed disproportionation of carbon monoxide. *Chem Phys Lett* 1996;260:471–5.
- [2] Jourdain V, Bichara C. Current understanding of the growth of carbon nanotubes in catalytic chemical vapour deposition. *Carbon* 2013;58:2–39.
- [3] Paillet M, Jourdain V, Poncharal P, Sauvajol JL, Zahab A, Meyer JC, et al. Growth and physical properties of individual single-walled carbon nanotubes. *Diamond Relat Mater* 2005;14(9):1426–31.

[4] Cheung CL, Kurtz A, Park H, Lieber CM. Diameter-controlled synthesis of carbon nanotubes. *J Phys Chem B* 2002;106:2429–33.

[5] Yoshida H, Takeda S, Uchiyama T, Kohno H, Homma Y. Atomic-scale in-situ observation of carbon nanotube growth from solid state iron carbide nanoparticles. *Nano Lett* 2008;8(7):2082–6.

[6] Li N, Wang X, Ren F, Haller GL, Pfefferle LD. Diameter tuning of single-walled carbon nanotubes with reaction temperature using a Co monometallic catalyst. *J Phys Chem C* 2009;113(23):10070–8.

[7] Jeong GH, Suzuki S, Kobayashi Y, Yamazaki A, Yoshimura H, Homma Y. Size control of catalytic nanoparticles by thermal treatment and its application to diameter control of single-walled carbon nanotubes. *Appl Phys Lett* 2007;90:043108.

[8] Pisana S, Cantoro M, Parvez A, Hofmann S, Ferrari A, Robertson J. The role of precursor gases on the surface restructuring of catalyst films during carbon nanotube growth. *Physica E* 2007;37(1):1–5.

[9] Noda S, Tsuji Y, Murakami Y, Maruyama S. Combinatorial method to prepare metal nanoparticles that catalyze the growth of single-walled carbon nanotubes. *Appl Phys Lett* 2005;86:173106.

[10] Hasegawa K, Noda S. Millimeter-tall single-walled carbon nanotubes rapidly grown with and without water. *ACS Nano* 2011;5(2):975–84.

[11] Kakehi K, Noda S, Maruyama S, Yamaguchi Y. Growth valley dividing single-and multi-walled carbon nanotubes: combinatorial study of nominal thickness of Co catalyst. *Jpn J Appl Phys* 2008;47(4):1961–5.

[12] Lu C, Liu J. Controlling the diameter of carbon nanotubes in chemical vapor deposition method by carbon feeding. *J Phys Chem B* 2006;110(41):20254–7.

[13] Jourdain V, Paillet M, Almairac R, Loiseau A, Bernier P. Relevant synthesis parameters for the sequential catalytic growth of carbon nanotubes. *J Phys Chem B* 2005;109(4):1380–6.

[14] Picher M, Anglaret E, Arenal R, Jourdain V. Processes controlling the diameter distribution of single-walled carbon nanotubes during catalytic chemical vapor deposition. *ACS Nano* 2011;5:2118–25.

[15] Picher M, Anglaret E, Arenal R, Jourdain V. Self-deactivation of single-walled carbon nanotube growth studied by in situ Raman measurements. *Nano Lett* 2009;9(2):542–7.

[16] Picher M, Anglaret E, Jourdain V. High temperature activation and deactivation of single-walled carbon nanotube growth investigated by in situ Raman measurements. *Diamond Relat Mater* 2010;19(5–6):581–5.

[17] Diarra M, Zappelli A, Amara H, Ducastelle F, Bichara C. Importance of carbon solubility and wetting properties of nickel nanoparticles for single wall nanotube growth. *Phys Rev Lett* 2012;109(18):185501.

[18] Lucchese M, Stavale F, Ferreira E, Vilani C, Moutinho M, Capaz RB, et al. Quantifying ion-induced defects and Raman relaxation length in graphene. *Carbon* 2010;48(5):1592–7.

[19] Navas H, Picher M, Arenal R, Quesnel E, Anglaret E, Jourdain V. Controlling the Crystalline Quality and the Purity of Single-walled Carbon Nanotubes Grown by Catalytic Chemical Vapor Deposition. *MRS Online Proceedings Library*, vol. 1515; 2013.

[20] Petitto S, Langell M. Surface composition and structure of  $\text{Co}_3\text{O}_4$  (110) and the effect of impurity segregation. *J Vac Sci Technol, A* 2004;22:1690.

[21] Hassel M, Freund H-J. High resolution XPS study of a thin CoO (111) film grown on Co (0001). *Surf Sci Spectra* 1996;4:273.

[22] Backman LB, Rautiainen A, Lindblad M, Jylhä O, Krause AO. Characterisation of Co/SiO<sub>2</sub> catalysts prepared from Co(acac)<sub>3</sub> by gas phase deposition. *Appl Catal A* 2001;208:223–34.

[23] Diehl F, Khodakov AY. Promotion of cobalt Fischer–Tropsch catalysts with noble metals: a review. *Oil Gas Sci Technol–Revue de l'IFP* 2009;64(1):11–24.

[24] Moteki T, Murakami Y, Noda S, Maruyama S, Okubo T. Zeolite surface as a catalyst support material for synthesis of single-walled carbon nanotubes. *J Phys Chem C* 2011;115(49):24231–7.

[25] Hwang IY, Kim JH, Oh SK, Kang HJ, Lee YS. Ultrathin cobalt silicide film formation on Si(100). *Surf Interface Anal* 2003;35(2):184–7.

[26] Coulter KE, Sault AG. Effects of activation on the surface properties of silica-supported cobalt catalysts. *J Catal* 1995;154(1):56–64.

[27] Girardon J-S, Lermontov AS, Gengembre L, Chernavskii PA, Griboval-Constant A, Khodakov AY. Effect of cobalt precursor and pretreatment conditions on the structure and catalytic performance of cobalt silica-supported Fischer–Tropsch catalysts. *J Catal* 2005;230(2):339–52.

[28] Ming H, Baker BG. Characterization of cobalt Fischer–Tropsch catalysts I. Unpromoted cobalt-silica gel catalysts. *Appl Catal A* 1995;123(1):23–36.

[29] Fouquet M, Bayer BC, Esconjauregui S, Blume R, Warner JH, Hofmann S, et al. Highly chiral-selective growth of single-walled carbon nanotubes with a simple monometallic Co catalyst. *Phys Rev B* 2012;85(23):235411.

[30] Li N, Wang X, Derrouiche S, Haller GL, Pfefferle LD. Role of surface cobalt silicate in single-walled carbon nanotube synthesis from silica-supported cobalt catalysts. *ACS Nano* 2010;4(3):1759–67.

[31] Lim S, Ciuparu D, Chen Y, Pfefferle L, Haller GL. Effect of Co-MCM-41 conversion to cobalt silicate for catalytic growth of single wall carbon nanotubes. *J Phys Chem B* 2004;108(52):20095–101.

[32] Jeong GH, Olofsson N, Falk LKL, Campbell EEB. Effect of catalyst pattern geometry on the growth of vertically aligned carbon nanotube arrays. *Carbon* 2009;47(3):696–704.

[33] Hasegawa K, Noda S. Moderating carbon supply and suppressing Ostwald ripening of catalyst particles to produce 4.5-mm-tall single-walled carbon nanotube forests. *Carbon* 2011;49(13):4497–504.

[34] Yun Y, Shanov V, Tu Y, Subramaniam S, Schulz MJ. Growth mechanism of long aligned multiwall carbon nanotube arrays by water-assisted chemical vapor deposition. *J Phys Chem B* 2006;110(47):23920–5.

[35] Chernavskii P, Pankina G, Lunin V. The influence of preparation conditions on the size of Co particles in cobalt-deposited catalysts of the Fischer–Tropsch synthesis. *Russ J Phys Chem A* 2006;80(4):546–50.

[36] Petit P, Salem D, He M, Paillet M, Parret R, Sauvajol J-L, et al. Study of the thermal stability of supported catalytic nanoparticles for the growth of single-walled carbon nanotubes with narrow diameter distribution by chemical vapor deposition of methane. *J Phys Chem C* 2012;116(45):24123–9.

[37] Amama PB, Pint CL, McJilton L, Kim SM, Stach EA, Murray PT, et al. Role of water in super growth of single-walled carbon nanotube carpets. *Nano Lett* 2008;9(1):44–9.

[38] Kim SM, Pint CL, Amama PB, Hauge RH, Maruyama B, Stach EA. Catalyst and catalyst support morphology evolution in single-walled carbon nanotube supergrowth: growth deceleration and termination. *J Mater Res* 2010;25(10):1875–85.

[39] Amama PB, Pint CL, Kim SM, McJilton L, Eyink KG, Stach EA, et al. Influence of alumina type on the evolution and activity of alumina-supported Fe catalysts in single-walled carbon nanotube carpet growth. *ACS Nano* 2010;4(2):895–904.

Poster abstract (status: accepted): extended  
Conference NT 15, Nagoya, Japan, 2015/06/29 - 2015/07/03

*How evolve the diameter and chirality distribution of single-walled carbon nanotubes with the synthesis time in C-CVD*

Hugo Navas <sup>1</sup>, Vincent Jourdain <sup>1,\*</sup>, Thierry Michel <sup>1</sup>, Matthieu Picher <sup>1</sup>, Eric Anglaret <sup>1</sup>,  
Annick Loiseau <sup>2</sup>, Frédéric Fossard <sup>2</sup>, Etienne Quesnel <sup>3</sup>

<sup>1</sup> Laboratoire Charles Coulomb (L2C), UMR 5221 CNRS-Université de Montpellier,  
Montpellier, F-France.

<sup>2</sup> Laboratoire d'étude des microstructures, UMR 104 CNRS-ONERA, 29 av. de la Division  
Leclerc, 92322 Châtillon, F-France

<sup>3</sup> CEA-LITEN, 17 rue des martyrs, 38054 Grenoble cedex 9, F-France

\* [vincent.jourdain@umontpellier.fr](mailto:vincent.jourdain@umontpellier.fr)

**Abstract**

Controlling the diameter and chirality distribution of single-walled carbon nanotubes (SWCNT) is crucial for their large-scale application. Although Catalytic Chemical Vapour Deposition (CCVD) is the most popular method for synthesizing SWCNTs, CCVD-grown SWCNTs usually present a large distribution of diameters and chiral angles. Several works have been devoted to understand and control the processes at the origin of this distribution. We previously evidenced several processes hindering the growth of small-diameter SWCNTs: catalyst coarsening, absence of nucleation, catalyst poisoning.<sup>1,2</sup> Here, we report on the evolution of the diameter and chirality distribution of SWCNTs with the synthesis time using two different approaches: *in situ* Raman monitoring and *ex situ* Raman characterization of samples frozen at different times. In most cases, the diameter distribution of SWCNTs is observed to significantly evolve with time (Figure 1). The type of evolution (e.g. toward smaller or larger diameters) strongly depends on the growth conditions (Figure 2). Post-growth analyses by HRTEM were performed to determine the underlying processes. Beside the evolution of diameter, we will also discuss how the evolution of the RBM inform on the evolution of the chirality distribution during CCVD.

**Introduction**

Single-walled carbon nanotubes (SWCNTs) display optical, electrical and chemical properties which are extremely dependent on their crystal structure and, most notably, of their diameter. Controlling the diameter distribution of single-walled carbon nanotubes (SWCNTs) is therefore a critical step toward the large-scale application of these one-dimensional nanostructures. Catalytic chemical vapor deposition (CCVD) is currently the most popular method for synthesizing SWCNTs due to its relatively good control of the growth conditions (catalyst, temperature, carbon supply and additives). A major drawback of CCVD is that SWCNT samples usually present a large distribution of diameters and chiral angles. Several works have been devoted to understand the processes at the origin of this distribution and the influence of the growth conditions on them. Our group notably evidenced that the growth of small-diameter SWCNT was limited to a narrow range of growth conditions because of three processes: i) the coarsening of small catalyst particles at too high temperature, ii) the absence of nucleation on small catalyst particles at too low carbon precursor pressure, iii) the poisoning

of small catalyst particles by carbonaceous materials at too high precursor pressure and too low temperature. Several groups developed catalysts and growth protocols achieving a high selectivity for specific ranges of diameters, chiral angles and crystal structures.

Here, we report on the evolution of the diameter distribution of SWCNTs as a function of the synthesis time using standard cobalt/silica and nickel/silica catalysts. Our study was based on Raman spectroscopy in both *in situ* and *ex situ* configurations. We show that in most conditions the diameter distribution strongly evolves with the synthesis time. Different types of evolutions are observed (e.g. toward smaller/larger diameters, no evolution), each prevailing in a specific set of growth conditions. Post-growth analyses of the samples by high-resolution TEM were performed to determine the origin of each behavior.

## Materials and Methods

10 nm layers of SiO<sub>2</sub> were deposited by Ion Beam Sputtering (IBS) on Si-wafers. 0.5 nm layers of catalyst (cobalt or nickel) were then deposited by IBS, measured with a quartz balance. The samples were calcined in air at 700°C before synthesis to remove carbon contaminants. This treatment roughens the surface and form catalyst particles suitable for CNTs growth. CCVD synthesis were performed in a cold-wall micro reactor Linkam TS1500 allowing *in-situ* Raman spectroscopy. *In-situ* and *ex-situ* micro-Raman measurements were performed at 647 nm (1.92 eV) and 532 nm (2.33 eV) with a Horiba Jobin Yvon T64000 equipped with a microscope. With a 50x objective, the laser spot on the sample is about 2  $\mu$ m. Ethanol was used as carbon precursor by bubbling argon (Air Liquid 99,999%) through a flask of liquid ethanol (Fluka, 99,8%) thermostated at 0°C. An additional argon line was used to dilute the gas mixture. The total gas flow was set at 1422 sccm.

## Results

To start this study, we monitored the evolution of the RBM profile during SWCNT growth by *in situ* Raman spectroscopy. Figure 1 shows three different types of observed evolutions of the RBM profile. The studied system is cobalt/SiO<sub>2</sub>. Fig. 1a illustrates an evolution from large-diameter SWCNTs to smaller SWCNTs and then larger SWCNTs at longer times. Fig. 1b illustrates the case where the RBM profile displays no marked evolution during the growth. These evolutions can also be visualized by plotting the ratio of the integrated intensities of small-diameter RBMs to those of large-diameter ones as a function of the synthesis time.

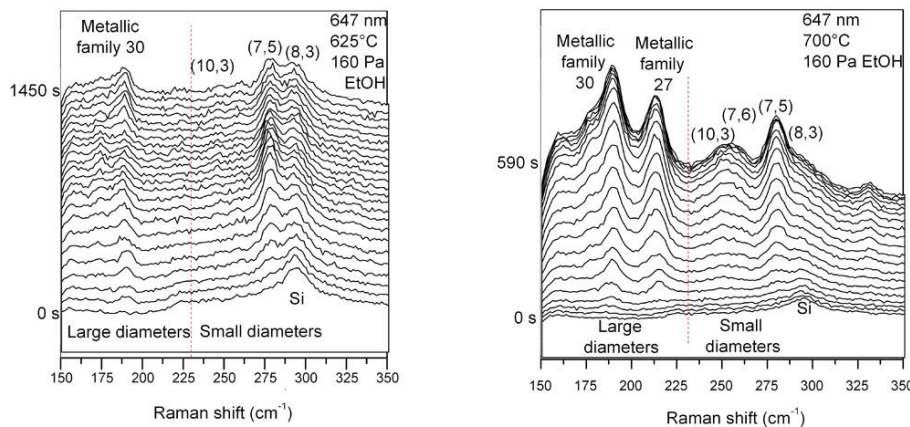


Figure 1. Evolution of the Raman spectra of SWCNTs during their growth monitored by *in situ* Raman measurements.

*In situ* Raman monitoring of the RBM profile represents a high-throughput approach in order to rapidly identify the different types of behaviors as a function of the growth conditions. However, it is limited to growth conditions providing a SWCNT yield sufficiently high for the

RBM to be measured in situ at high temperature (600-800°C) and short acquisition times (1-30 s). This approach is therefore not adapted to explore the extreme regions of the growth domain displaying a low yield, most especially the low temperatures and low precursor pressures. For studying the nickel/silica catalyst, we adopted a different but complementary approach based on freezing the samples at different synthesis times (by stopping the carbon precursor supply and rapidly cooling the cell) then performing a detailed Raman characterization at room temperature. This approach provides higher resolution spectra but also a better statistical analysis by allowing to average Raman spectra recorded at different positions on the sample. In order to check the generality of our observations, we also used a different laser wavelength ( $\lambda=532$  nm) in order to be in resonance with a different set of SWCNTs.

Figure 2 illustrates typical Raman spectra obtained in such experiments.

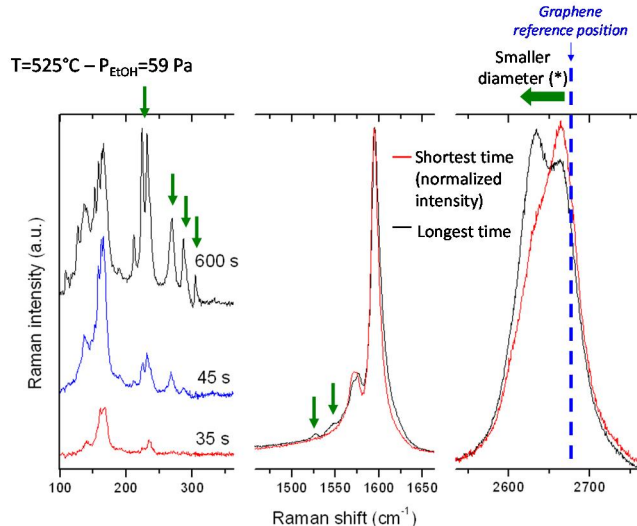


Figure 2. Evolution of the Raman spectra of SWCNTs for syntheses frozen at different times.

Figure 3 summarizes in which growth conditions are observed the different behaviors.

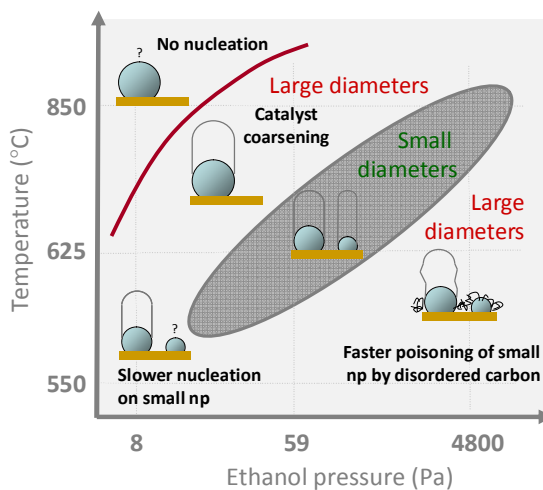


Figure 3. Processes responsible for the evolution of the diameter distribution of SWCNT during CCVD growth.

## References

1. Picher et al, ACS Nano 2011. **5**, 2118
2. Navas et al, Carbon 2014 **80**, 599

# **Oxidation Mechanism of Individual Single-Walled Carbon Nanotubes on Substrate Monitored by *in situ* Scanning Electron Microscopy**

Hasan-al Mehedi<sup>1</sup>, Johann Ravaux<sup>2</sup>, Khadija Yazda<sup>1</sup>, Thierry Michel<sup>1</sup>, Saïd Tahir<sup>1</sup>, Michaël Odorico<sup>2</sup>, Renaud Podor<sup>2</sup>, Vincent Jourdain<sup>1,\*</sup>

<sup>1</sup>**Laboratoire Charles Coulomb (L2C), UMR 5221 CNRS-Université de Montpellier, Montpellier, F-France.**

<sup>2</sup>**Institut de Chimie Séparative de Marcoule, UMR 5257 CEA-CNRS-UM2-ENSCM Site de Marcoule, Bat 426, BP 17171, F-30207 Bagnols sur Cèze cedex**

## **Abstract**

We report a direct study on the oxidation of individual single-walled carbon nanotubes (SWCNTs) deposited on substrates in oxygen gas at temperatures between 480 and 580 °C, as we continuously locate and identify the modifications along the same individual SWCNTs as they undergo oxidation. The nanotubes are observed to disappear segment-by-segment during the *in situ* observations at the resolution of an environmental scanning electron microscope (ESEM). Additional atomic force microscopy (AFM) characterization of the nanotubes before and after oxidation reveals that the nanotube oxidation is associated with both cutting and etching of the tubes where semiconducting SWCNTs is preferentially cut and etched. The origin of this selectivity is explained by the effect of substrate-trapped charges and electron beam induced surface charging. A mechanism underlying the oxidation of charged SWCNTs deposited on substrates is also proposed.

## **Introduction**

Understanding the mechanisms underlying the oxidation of carbon nanotubes (CNTs) is of great importance for their synthesis and post-processing, and the behavior of CNT-based devices. For instance, CNTs were found to exhibit lower emission currents and reduced lifetimes in low pressures of oxygen and water vapor due to reactive sputter etching.<sup>1,2</sup> Gas-phase oxidizers such as CO and water vapor are frequently used during CNT growth to selectively burn off amorphous carbon by-products in order to enhance and preserve catalyst activity.<sup>3-7</sup> Thermally oxidizing CNT material in air or oxygen is also routinely performed to remove unwanted disordered carbon materials or create oxygen-containing moieties on CNT walls.<sup>3-12</sup> Several groups already

attempted to utilize the oxidation process to manipulate CNT structures, for instance by opening up their terminating cap or by thinning the tubes.<sup>13,14</sup> When controlled, oxidation therefore plays an important role in the synthesis, modification and purification of CNTs.

Unlike solution-based sorting, gas-phase purification of CNTs does not result in residues and thereby, leaves nanotubes in a pristine state. Recently there has been a resurgence of interest in oxidative purification of SWCNTs with respect to semiconducting or metal type. SWCNTs can be metallic or semiconducting depending on their chiral angles.<sup>15,16</sup> Many valuable applications in, for example transparent conductors,<sup>17</sup> solar cells,<sup>18</sup> biosensors,<sup>19</sup> and nanoelectronics<sup>20</sup> require individualized SWCNTs of specific electronic character (metallic/semiconducting SWCNTs) and high purity. Despite recent progress in selective synthesis, current techniques still produce heterogeneous samples containing SWCNTs of varying geometry and electronic character as well as other carbonaceous contaminants.<sup>21,22</sup> Post-processing of as-synthesized SWCNTs, on the other hand, is suggested to be an alternative approach for the type-selective isolation of SWCNTs, and there is already evidence that separation can be achieved using various gas-phase oxidants including air,<sup>23,24</sup> O<sub>2</sub>,<sup>5,11,23-27</sup> SO<sub>3</sub>,<sup>6</sup> water vapor,<sup>28</sup> and fluorine gas.<sup>29</sup> Depending on the oxidants and the particular treatment, either metallic (m-CNTs)<sup>29-31</sup> or semiconducting nanotubes (s-CNTs)<sup>32,33</sup> are observed to be etched preferentially. Oxidation rates were found to increase with smaller CNT diameter which was typically explained in terms of higher C-C bond strain and higher sp<sup>3</sup> character resulting in higher chemical reactivity towards adsorbates.<sup>23-28,34-38</sup> Density functional theory-based calculations, however, suggest that it is the local curvature radius (LCR) that determines the weakest carbon-carbon bond and is consequently thought to be one of the determining factors in oxidative etching.<sup>23,35</sup> Other studies have shown that chirality is expected to have a direct effect on oxygen sidewall chemisorptions and can affect chemical reactivity in general.<sup>39,40</sup> Preferential m-CNT etching is attributed to the finite density of states (DOS) at the Fermi level for m-CNTs whereas hole doping was reported to enhance the chemical reactivity of s-CNTs and lead to their preferential etching.<sup>33</sup> Chemical doping induced by the substrate is also to be considered as illustrated by its strong influence on the oxidation of monolayer graphene deposited on substrates.<sup>41</sup>

In all previous studies, the oxidation of CNTs was usually characterized by *ex situ* measurements on ensembles of SWCNTs. *In situ* approaches at the level of individual SWCNTs are well suited for investigating CNT oxidation, as one can track the dynamics of the process as it happens and

observe trends that might be difficult to detect in *ex situ* ensemble measurements. For instance, earlier studies have suggested that CNT oxidation initiates at the end of the tube and proceeds along its length.<sup>13,14</sup> Recent *in situ* environmental transmission electron microscopy (ETEM) investigation of multi-walled CNT oxidation, on the other hand, reveals that despite the higher curvature of the carbon cap, it is the outer wall which is oxidized and etched first.<sup>39</sup>

In this article, we report a direct study on the oxidation of individual SWCNTs deposited on substrates in oxygen gas at temperatures between 480 and 580 °C at the resolution of an environmental SEM. By this *in situ* approach, we could continuously locate and identify the modifications along the same individual SWCNTs as they undergo oxidation. Most notably, SWCNTs are observed to disappear segment-by-segment during the *in situ* SEM observations. Additional AFM characterization of the SWCNTs before and after oxidation reveals that SWCNT oxidation is associated with both cutting and etching of the tubes. The oxidation mechanism is investigated as a function of the temperature and of the substrate type (quartz and SiO<sub>2</sub>/Si). In our experimental conditions, SWCNT oxidation by O<sub>2</sub> is found to be type-selective with semiconducting SWCNTs being preferentially cut and etched. The origin of this selectivity is discussed, and a mechanism underlying the oxidation of charged SWCNTs deposited on substrates is proposed.

## RESULTS

The CNTs investigated in this work are grown on ST-cut quartz wafers by catalytic chemical vapor deposition, as described elsewhere.<sup>42</sup> An SEM image of the as-synthesized CNT arrays on a quartz substrate is shown in Figure 1a. The nanotubes are straight, long (length ranges from 30 to 170 μm) and horizontally-aligned along the X-direction of the ST-cut quartz substrate. Each tube has one end connected to the catalyst line (that consists of entangled CNTs) while its other end is free from any connection. Prior to oxidation, some CNT samples were characterized by Raman spectroscopy using a 532 nm laser excitation. To facilitate the characterization, the nanotubes were transferred on a SiO<sub>2</sub>/Si substrate. The transfer process (detailed in the Methods section) can induce curls along the tubes (Figure 1b) due to the release of the pressure developed into the CNTs during growth and to the instabilities in the liquid phase. Figures 1c and 1d show the Raman spectra of a typical CNT sample and reveal that the CNTs are mostly single-walled with diameters ranging from 1.3 to 1.7 nm. The average I<sub>D</sub>/I<sub>G</sub> ratio is about 0.03 indicating a very low density of defects.

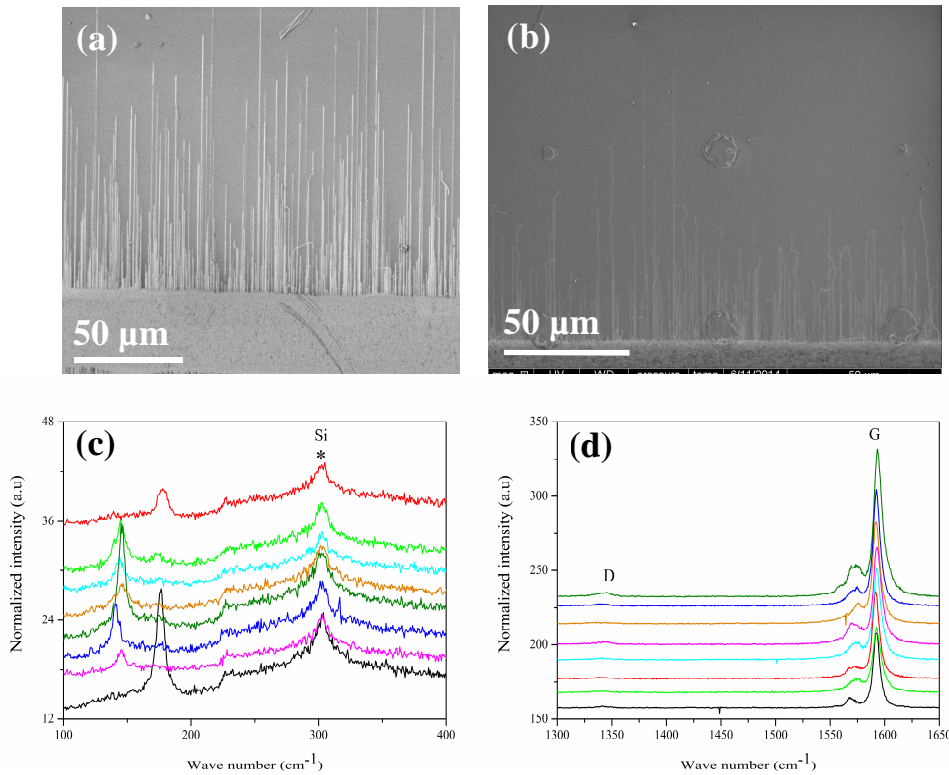


Figure 1. SEM images of (a) as-synthesized SWCNTs on ST-cut quartz and (b) SWCNTs transferred on  $\text{SiO}_2/\text{Si}$  substrates. Raman spectra of SWCNTs transferred on  $\text{SiO}_2/\text{Si}$ : (c) RBM region and (d) G and D mode region recorded using a 532 nm laser wavelength.

During our *in situ* SEM experiments, the nanotubes are first imaged at room temperature in vacuum ( $<10^{-2}$  Pa) prior to oxidation. The ESEM image of the as-synthesized SWCNTs on a selected part of the quartz substrate at higher magnification (Figure 2a) clearly shows that some tubes appear very bright while other ones are much darker.

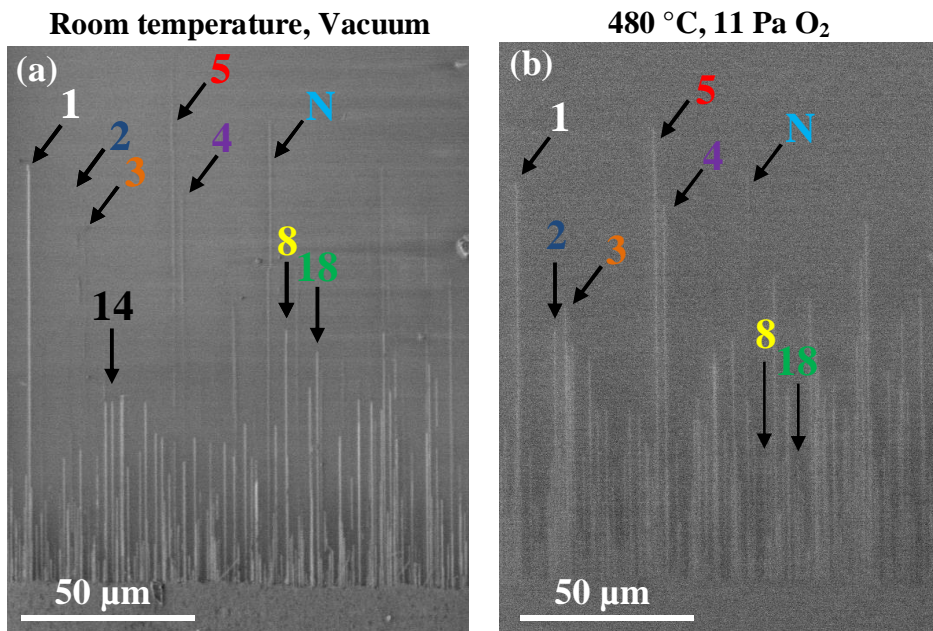


Figure 2. SEM images of as-synthesized SWCNTs on a quartz substrate (a) at room temperature in  $10^{-2}$  Pa before oxidation and (b) at 480 °C after 190 s of exposure to 11 Pa of pure O<sub>2</sub>. The images were recorded using an accelerating voltage of 1.8 kV.

Individual SWCNTs deposited on insulating substrates can be imaged by SEM, thanks to the surface charge contrast induced by the electrical conductivity of SWCNTs.<sup>43</sup> The contrast is strongly enhanced if the tube is connected to an electrode so that the charges induced by the electron beam can be efficiently evacuated away from the imaged area. In our case, the catalyst line which consists of a network of entangled and conducting SWCNTs plays such a role. Recent work indicates that the contrast of SWCNTs in SEM images is also related to their electrical properties, the brighter and the darker SWCNTs corresponding respectively to metallic and semiconducting SWCNTs.<sup>44</sup> This M/SC contrast is clearest if all the tubes are connected to the same electrode (*i.e.* the catalyst line in our case). In Figure 2, one can assign the SWCNTs marked as 2, 3, 4 and 5 as semiconducting whereas SWCNTs marked as 1, 8, 14 and 18 are metallic.

The SEM image in Figure 2b corresponds to the same region recorded at 480 °C, 190 s after the introduction of oxygen into the chamber. As apparent, most tubes now appear equally bright which we attribute to the electrical conductivities of semiconducting and metallic SWCNTs becoming closer with increasing temperature.<sup>45,46</sup> The very few tubes which still appear dark at high temperature (e.g. tube N in Figure 2b) could correspond to small-diameter semiconducting SWCNTs remaining poorly conducting at high temperature due to their larger band gap. These

observations provide an additional support to the metallic/semiconducting assignment based on SEM contrast. After O<sub>2</sub> injection, several tens of seconds were usually required to adjust the imaging parameters and to obtain the first image in oxidizing conditions. In this first image, several tubes are already observed to be shorter than at room temperature (e.g. tubes marked by 2, 3, 5, 8 and 18) due to the exposure to oxygen at high temperature. Movie S1 (in Supporting Information) illustrates the evolution of the CNTs shown in Figure 2 with the time of exposure to oxygen (480 °C, 11 Pa of O<sub>2</sub>). Figure 3 shows a few snapshots of the movie at different times in a specific zone (left part of Figure 2).

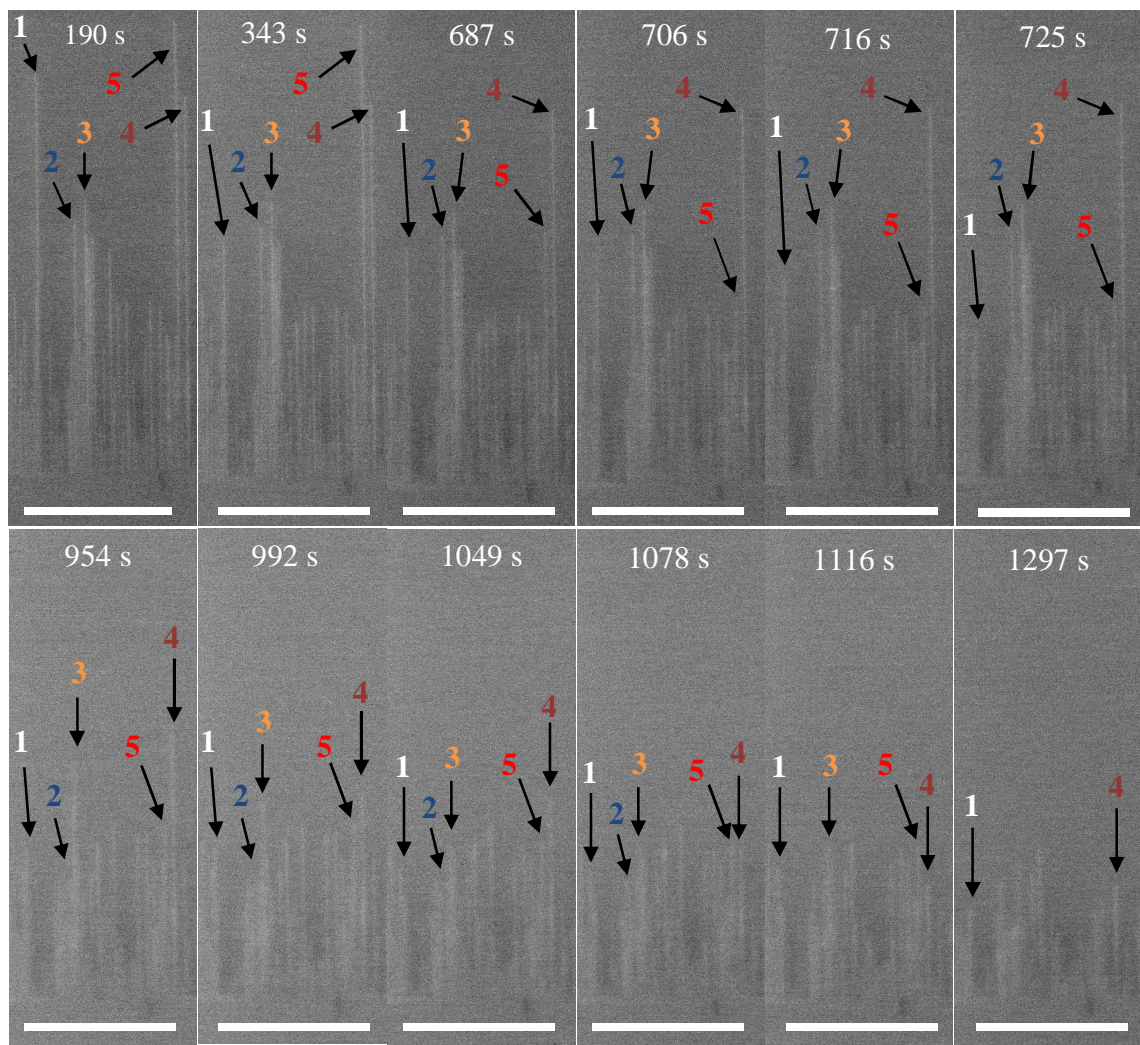


Figure 3. *In situ* SEM images of SWCNTs on a quartz substrate during oxidation in 11 Pa O<sub>2</sub> at 480 °C illustrating the segment-by-segment disappearance of the CNTs with time. The scale bar is 50 μm.

As shown in Movie S1 and in Figure 3, the apparent length of each nanotube decreases with time. The most striking feature of our *in situ* observations is that the nanotube length does not decrease progressively as would be expected from a continuous nanotube etching from one end but instead decreases sequentially (*i.e.* segment by segment). Another feature of our observations is that the segments are always apparently removed from the free end of the tube. Three different hypotheses can be proposed to explain these observations:

(I) *Local cutting.* In this hypothesis, the oxidation would induce a local cutting of the tube (preferentially at a pre-existing defective site) resulting in two nanotube segments: the segment still connected to the catalyst line would remain visible while the other one would disappear from the SEM picture because of its disconnection from the catalyst line.

(II) *Fast etching and abrupt stop.* Here, the oxidation would induce a rapid and continuous etching of the tube starting from the nanotube end until a certain position along the tube (*e.g.* a pre-existing defect) where the etching would abruptly stop; here it is hypothesized that the etching is too fast to be resolved at the acquisition rate of the SEM pictures.

(III) *Bunch of nanotubes.* In this scenario, the observed line would actually consist of several tubes of different lengths which are too close to be resolved by SEM (*e.g.* a nanotube bundle); the abrupt disappearance of one segment would be caused by either the fast etching or the local cutting of the longest tube of the bunch.

To test each of these three hypotheses, we performed AFM characterization on one randomly selected zone of a given sample before and after monitoring its oxidation by *in situ* SEM. Figures 4a and 4b show SEM images of the zone before and after 17 min of oxidation, respectively. The tubes in this zone are marked with letters ranging from A to L. Although G and J appear as single lines in the SEM picture, AFM reveals that each of them actually consists of two neighboring tubes of different lengths that we labeled as G(1,2) and J(1,2), respectively. Note that, although the oxidation behavior of each of these four tubes cannot be monitored by *in situ* SEM, it can be characterized by *ex situ* AFM. The characteristics of all these tubes (length, type) and the corresponding oxidation behavior are listed in Table ST1.

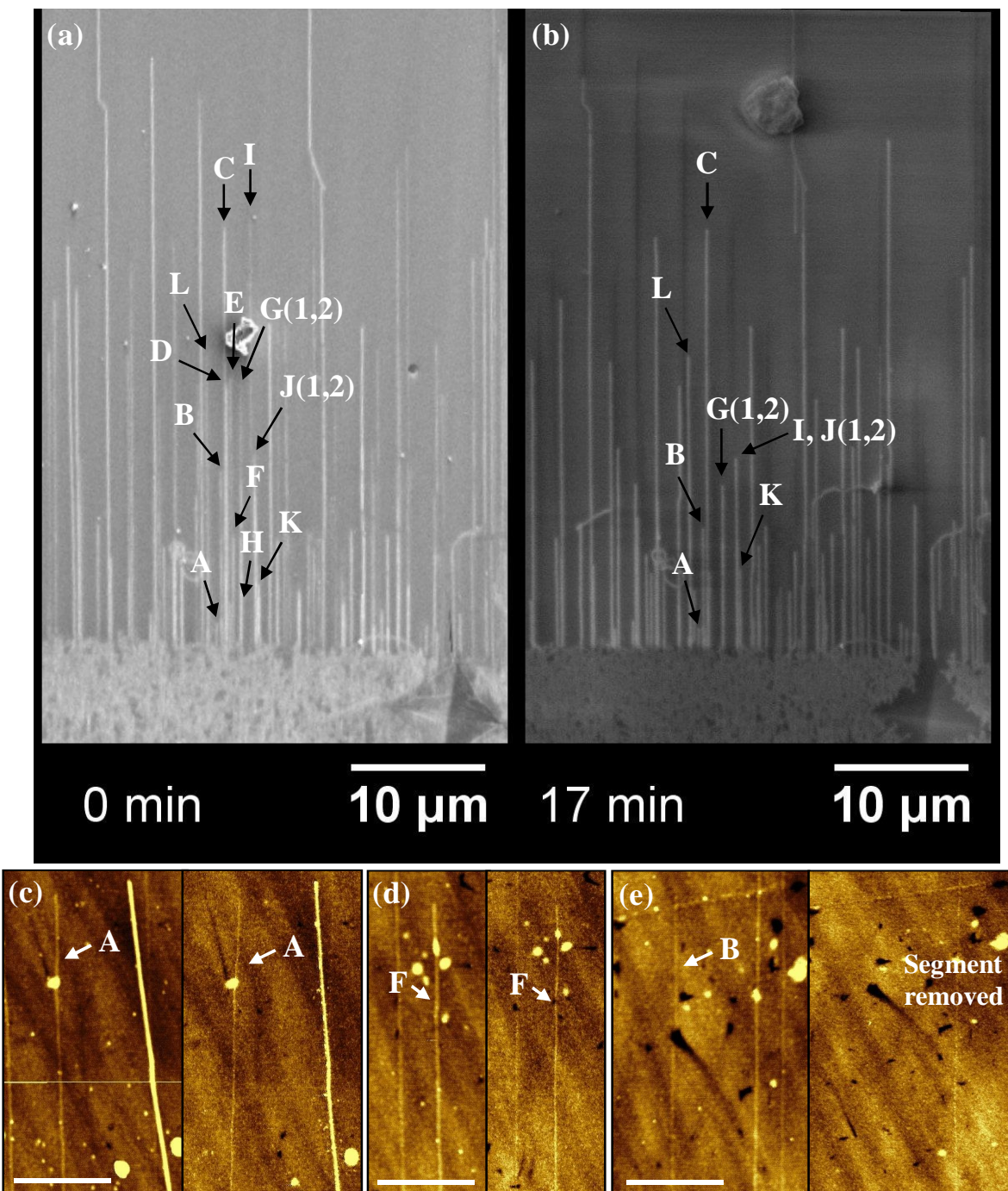


Figure 4. SEM images of the randomly selected zone of a given sample (a) before oxidation and (b) after 17 min of oxidation at 540 °C. The labeled tubes are characterized by AFM. (c-e) AFM images of individual SWCNTs on quartz substrate before and after oxidation displaying three types of oxidation behavior: (c) no change, (d) disappeared segment in the SEM picture appears in the AFM picture and (e) segment physically removed. Scale bar for AFM images is 500 nm.

The observed behaviors can be categorized as follows:

**No length change in SEM and AFM.** Several tubes (tubes A, C, J(1,2), K and L) displayed no apparent reduction of their lengths during *in situ* observations and still appeared in the AFM images with unchanged lengths. AFM pictures of tube A before and after oxidation are shown in Figure 4c to illustrate this type of SWCNTs having a very low reactivity.

**Length change in SEM but not in AFM.** We observed one tube (tube F) displaying the features of hypothesis I, that is, the segment which disappeared during the SEM observations still appeared with unchanged length in the AFM picture after oxidation (Figure 4d). This observation agrees with a local cutting of the tube causing a disappearance of the disconnected segment during the ESEM observations. The existence of this mechanism is additionally supported by *in situ* observations of segments blinking for a few seconds before complete disappearance (see Movie S2 in supporting info). Note that despite our attempts, we were not able to identify by AFM a cut along the nanotube at the position expected from the SEM picture. We presume that this is because the width of the cut is under the lateral resolution of our AFM setup.

**Same length change in both SEM and AFM.** Finally, several tubes displayed the features of hypothesis II (tubes B, D, E and G(1,2)), that is segments which disappeared during the *in situ* SEM observations are found to be physically removed (etched) in the AFM images (Figure 4e).

Note that we observed one tube (tube I) which displayed consecutive disappearance of two segments during *in situ* observation and exhibited two types of behavior, *i.e.* the AFM characterization revealed that the first segment was physically removed while the second segment was still present on the substrate. This case supports that local cutting (mechanism I) may systematically precede the rapid etching of the disconnected segment (mechanism II). This would notably explain why we only observed abrupt disappearances of tube segments and why we never observed the progressive etching of a nanotube as would be expected from mechanism II alone. If so, this also raises the question of why disconnected segments would be more rapidly etched than connected ones.

To test hypothesis III (bunch of nanotubes), we searched by AFM for evidence of nanotube bundling or of changes of geometrical features (width or height) along the nanotubes at the positions where the segments were observed to be removed during the *in situ* observations. All our observations support that the studied tubes on quartz are single and have a constant diameter all

along their length. So, even though hypothesis III cannot be completely excluded, it finds no experimental support in the AFM data.

For a quantitative analysis, the recorded *in situ* images were analyzed to extract the number of segment disappearance (cutting events) as a function of time and the cutting position along the nanotubes. The corresponding SEM images and extracted data are summarized in Figures S1-4 and Tables ST2-5 in the SI.

First, the analysis shows that there is no preferential position of cutting along the CNTs (that is closer to the free end or closer to the catalyst line). When averaged over a large number of cuttings, the average cutting position with regard to the initial length of the tube is close to the middle of the tube (see Table ST2-5). The cuts therefore appear at random positions along the nanotubes. Second, the average time between two consecutive cutting events tends to increase when the total length of remaining tubes decreases (Figure S5). Third, if normalized by the sum of the remaining nanotube lengths, the number of cutting events at a given time tends to increase with time (Figure S6).

These observations support that the probability of a cutting event is proportional to the tube length and to the time of exposure to oxygen. To account for these trends at the individual nanotube level, we defined the index of reactivity ( $R$ ) of an individual nanotube as:

$$\lim_{n_j \rightarrow +\infty} \left[ \frac{\sum_{i=1}^{i=n^j} \frac{1}{\Delta t_i^j L_{i-1}^j}}{n_j} \right] = R^j$$

where  $L_i^j$  is the length of the individual tube  $j$  after the  $i^{\text{th}}$  cutting event,  $\Delta t_i^j$  is the interval of time between the  $(i-1)^{\text{th}}$  cut and the  $i^{\text{th}}$  cutting event of tube  $j$ , and  $n^j(t)$  is the total number of cutting events experienced by tube  $j$  after time  $t$ . Experimentally, we do not have access to an infinite number of cutting events but we found that the index converges towards a quite constant value for a number of cutting events typically greater than 4 (Figure S7).

Similarly, the average reactivity  $R^{\text{ensemble}}$  of a collection of nanotubes during a given experiment can be defined as:

$$\lim_{t \rightarrow +\infty} \left[ \frac{\sum_{\text{all tubes}} \frac{1}{\Delta t_i^j L_{i-1}^j}}{n^{\text{ensemble}}(t)} \right] = R^{\text{ensemble}}$$

where  $n^{\text{ensemble}}(t)$  is the total number of cutting events experienced by the nanotube collection after time  $t$ . For statistical validity, we also checked that  $R^{\text{ensemble}}$  converges towards a constant value within the time scale of the experiment (Figure S8).

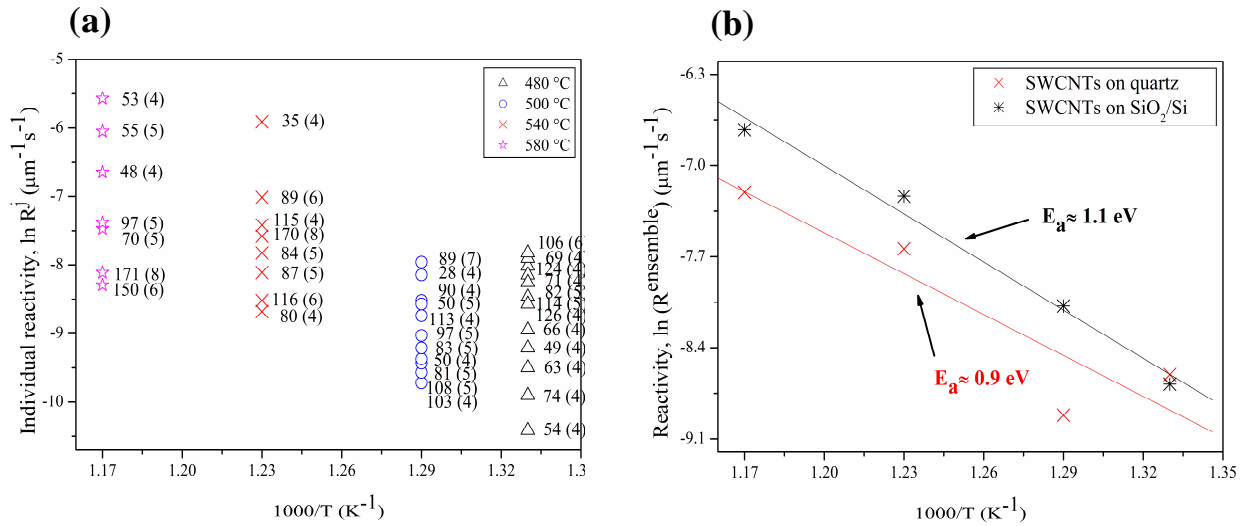


Figure 5. Variation of reactivity of (a) individual and (b) ensemble SWCNTs with oxidation temperatures. In figure (a), individual reactivities are displayed for SWCNTs on quartz. The first number before the brackets correspond to the initial length of the nanotubes in  $\mu\text{m}$ ; the numbers within brackets indicate the total number of cutting events for each individual nanotube (for statistical validity, nanotubes displaying less than 4 cutting events are not included).

As shown in Figure 5a, the individual reactivities, while largely scattered, tend to increase with increasing temperature. The ensemble reactivity tends to follow an Arrhenius law with an activation energy of about 1 eV (0.9 eV on crystalline quartz, 1.1 eV on amorphous thermal SiO<sub>2</sub> on Si, see Figure 5b), which is of the order or slightly lower than the activation energy ( $\sim 1.2 \text{ eV}$ ) reported for monolayer etching of the basal plane of graphite in O<sub>2</sub>.

As previously mentioned, some tubes display many segment removals while other ones remain nearly unmodified within the timespan of the experiment. Such large differences of reactivity

suggest that the reactivity is strongly affected by the nanotube features such as the metallic/semiconducting (M/SC) type, the diameter and/or the density of defects.

The individual reactivity of fifteen tubes with varying lengths is compared in Table ST6 with respect to their M/SC types as ascribed from their SEM contrast (see Figures 2a and S1). As before, only tubes with a number of cutting events greater than 4 were used to ensure statistical validity. Please note that the least reactive tubes (i.e. with less than 4 cutting events) were therefore neglected in this first approach. The individual reactivities are quite scattered varying by a factor 10 for both metallic and semiconducting tubes. On average, the reactivity appears substantially higher for semiconducting tubes ( $\sim 2.6 \times 10^{-5} \mu\text{m}^{-1}\text{s}^{-1}$ ) than for metallic tubes ( $\sim 1.4 \times 10^{-5} \mu\text{m}^{-1}\text{s}^{-1}$ ), supporting a slightly higher reactivity of semiconducting tubes. This trend is also apparent in the coupled SEM-AFM experimental data (see Table ST1) where most metallic tubes display no cuts within the timespan of the experiment while most semiconducting tubes display 1 or 2 cuts. This highlights another approach for comparing the reactivities of metallic and semiconducting by considering the average number of cutting events experienced by metallic tubes and semiconducting tubes during the total duration of a given experiment. For such a measurement, eight semiconducting and twelve metallic tubes of a given experiment ( $T=480^\circ\text{C}$ ) were selected and their average numbers of cutting events were normalized by the total initial lengths of the tubes (639  $\mu\text{m}$  and 790  $\mu\text{m}$  for semiconducting and metallic tubes respectively) and by the duration of the experiment (45 min). This analysis again confirms that semiconducting tubes experienced slightly more cutting events ( $2.3 \times 10^{-5} \mu\text{m}^{-1}\text{s}^{-1}$ ) than metallic tubes ( $1.9 \times 10^{-5} \mu\text{m}^{-1}\text{s}^{-1}$ ) supporting again a slightly higher reactivity of semiconducting tubes.

In order to confirm the effect of the nanotube structural features (M/SC type, diameter and defect density) on their reactivity, we characterized several individual tubes of a given zone by Raman spectroscopy before monitoring their oxidation by *in situ* SEM. Unexpectedly, we observed that all tubes were oxidized extremely rapidly within the first tens of seconds of exposure to oxygen, whatever their type (M/SC) and diameter (Figure S9). This precluded the use of Raman spectroscopy to directly correlate the reactivities of individual SWCNTs with their structural features. Interestingly, these first cuttings preferentially appeared along the line the laser was scanned during Raman characterization. This prompted us to check the influence of the e-beam exposure on the SWCNT reactivity. To do so, we performed a long monitoring of SWCNT oxidation by ESEM in a given zone before zooming out in order to compare the reactivities in the

zones exposed and not exposed to the e-beam. As shown in Figure S10, e-beam exposure strongly accelerates the oxidation of SWCNTs by O<sub>2</sub>. From these observations, we conclude that local exposure to laser or electron beam can significantly increase the reactivity of SWCNTs deposited on substrates. Laser exposure is known to induce local modifications (chemical functionalization, optical doping) or even structural damages to SWCNTs and graphene, which would explain why the exposed areas became more reactive. The e-beam effect cannot be explained in terms of structural damages caused by the incident electrons since the accelerating voltage is well below the knock-on damage threshold for sp<sup>2</sup> carbons in a hexagonal network.<sup>47,48</sup> At the opposite, the most obvious effect of the e-beam exposure is to cause surface charging.

## DISCUSSION

The charging of an insulator surface under electron beam irradiation depends on the accelerating voltage which controls the ratio of secondary electrons emitted by the surface to incident electrons.<sup>49</sup> At high accelerating voltages, the SiO<sub>2</sub> surface is negatively charged and appears brighter than neutral SiO<sub>2</sub>; at accelerating voltages below a threshold value (typically 3 kV for a thin layer SiO<sub>2</sub> layer on Si and 10 kV for bulk quartz), the surface becomes positively charged and appears darker than an uncharged SiO<sub>2</sub> surface because its positive potential hinders the emission of secondary electrons.<sup>50</sup> At very low accelerating voltages (typically less than a few hundreds mV), the surface becomes negatively charged again. In our experimental conditions (V<sub>acc</sub>=1.8 kV), the SiO<sub>2</sub> surface is therefore positively charged and has a surface potential up to several volts. As shown by the group of Kaili Jiang<sup>51</sup>, the SWCNTs which are connected to an outer electrode (i.e. the catalyst line in our case) provide electrons to the surrounding SiO<sub>2</sub> surface making it appear brighter than the rest of the surface. It follows that the SiO<sub>2</sub> surface surrounding unconnected tubes has a high density of surface charges (holes) while the SiO<sub>2</sub> surface surrounding connected tubes is much less charged. At room temperature, the SiO<sub>2</sub> surface surrounding metallic tubes will be less charged than that surrounding semiconducting tubes, as evidenced by their different contrast in SEM. At the high temperatures used for the oxidation experiments (480-580°C), the conductivities of M and SC tubes become closer and so do the surface charge density of the SiO<sub>2</sub> surrounding them, as evidenced by the close SEM contrasts of M and SC tubes at these temperatures.

In the case of graphite or of several-layer graphene, oxidation is initiated at pre-existing point defects, which manifests by a rather low reactivity and a homogeneous size distribution of etch pits. However, in the case of monolayer graphene supported on a substrate, oxidation is strongly enhanced<sup>52</sup> which was explained by the effect of substrate-trapped charges<sup>41</sup> which cause spatial fluctuations of the Fermi energy, that is electron and hole puddles in graphene that alternate in space.<sup>53,54</sup>

We propose that a similar process is at work in our case during the oxidation of substrate-supported SWCNTs, and that it is amplified by the surface charging induced by the e-beam. Evidence of electron and hole puddles along quartz-supported SWCNTs can be found in many SEM pictures at room temperature displaying marked variations of contrast along individual semiconducting SWCNTs (see Figure S10 in the SI). Note that these contrast fluctuations cannot be observed at high temperature probably because of the higher charge mobility and to the lower signal to noise ratio in ESEM conditions.

To test the hypothesis that SWCNT oxidation is primarily controlled by substrate charges, we studied the oxidation kinetics of SWCNTs transferred from quartz to amorphous thermal silicon oxide (on Si) which is known to contain a higher density of sites for trapping surface charges.<sup>55,56</sup> As shown in Figure 5b, the SWCNT reactivity is higher on SiO<sub>2</sub>/Si substrates than on ST-cut quartz. The activation energies are quite similar on crystalline quartz and on amorphous SiO<sub>2</sub> (~1 eV) supporting that the chemical processes at play are the same on both substrates, and that the higher rate of oxidation on amorphous SiO<sub>2</sub> is caused by the higher density of surface-trapped charges.

As previously described, the density of surface charges is also considerably impacted during ESEM observations by the e-beam exposure and the electronic conductivity of SWCNTs. If SWCNT oxidation is primarily controlled by substrate charges, one would expect very different SWCNT reactivities depending on the actual surface charge density of the substrate below the nanotube. This is the case as illustrated by the two different oxidation behaviors we observed:

- i) slow oxidation manifesting by a local cutting for tube segments that are still connected to a reservoir of electrons (catalyst line),
- ii) rapid oxidation manifesting by a complete etching of the tube segments which have been disconnected from the catalyst line.

Based on these arguments, we propose the following oxidation mechanism for SWCNTs supported on substrates under e-beam exposure. SWCNTs deposited on  $\text{SiO}_2$  surfaces and exposed to air are slightly p-doped with a level of doping that can vary along the nanotube. Doping is higher for substrates able to stabilize a high density of surface ions. Laser exposure can locally modify the doping.<sup>57</sup> Doping affects the reactivity of m-SWCNTs because of their constant DOS. However, the reactivity of s-SWCNTs can be greatly enhanced at highly-doped areas by increasing the DOS close to the Fermi level. P-type doping is even enhanced under e-beam exposure and so is the reactivity of s-SWCNTs. Reactivity is further enhanced for segments of s-SWCNTs which become disconnected from other SWCNTs because of higher p-doping.

## Conclusion

We reported a direct study on the oxidation of individual single-walled carbon nanotubes (SWCNTs) deposited on substrates in oxygen gas at temperatures between 480 and 580 °C, as we continuously locate and identify the modifications along the same individual SWCNTs as they undergo oxidation. The nanotubes were observed to disappear segment-by-segment during the *in situ* observations at the resolution of an environmental scanning electron microscope (ESEM). Additional atomic force microscopy (AFM) characterization of the nanotubes before and after oxidation revealed that the nanotube oxidation is associated with both cutting and etching of the tubes where semiconducting SWCNTs are preferentially cut and etched. The origin of this selectivity is explained by the effect of substrate-trapped charges and electron beam induced surface charging. A mechanism underlying the oxidation of charged SWCNTs deposited on substrates has been proposed.

## Experimental

Two types of substrates were used: SWCNTs grown on stable temperature-cut (ST-cut) quartz wafers by catalytic chemical vapor deposition<sup>42</sup> and nanotubes transferred from the parent quartz substrates on Si substrates with a 500 nm layer of thermal  $\text{SiO}_2$ . Nanotubes were transferred on Si substrates first to facilitate their characterization by Raman spectroscopy (wavelength 532 nm, laser power 0.5 mW, objective 50X) before oxidation (to determine type of tubes, SWNTs/MWNTs; diameter distribution) and secondly to investigate any influence of the substrate on the oxidation kinetics. Briefly, transfer of SWCNTs from quartz substrates to the patterned

$\text{SiO}_2/\text{Si}$  substrates was carried out by a polymeric water-based method using cellulose acetate butyrate (CAB).<sup>58</sup> The quartz substrates with SWCNTs were spin-coated by a thin layer of cellulose acetate butyrate (CAB). After baking (50°C, 1 h), the CAB layer with embedded nanotubes was peeled from the quartz by soaking in ultrapure (Milli-Q) water overnight. The peeling occurs due to the intercalation of a layer of water molecules between the hydrophilic surface and the hydrophobic nanotubes embedded in the hydrophobic polymer (CAB). The peeled layer floating at the surface of water was then transferred onto silicon substrates ( $\text{SiO}_2/\text{Si}$ ) patterned with alignment markers (created and etched on the substrate by lithography using S1818 resin, a positive photoresist, and reactive-ion etching (RIE)) and baked (70°C, 1 h). The CAB layer was then removed by soaking in ethyl acetate solution (20 min), in acetone (5 min) and isopropanol (5 min).

The *in situ* oxidation experiments were performed using a Field Emission Gun Environmental Scanning Electron Microscope (ESEM, model FEI QUANTA 200 ESEM FEG) equipped with a heating cell (5 mm inner diameter MgO ceramic crucible, 25-1500 °C) under 11 Pa of  $\text{O}_2$  at temperatures in the range of 480-580 °C. The water cooling system of this device was associated to an expansion tank that limited the stage vibration during the experiment. A specific detector was used for *in situ* gaseous secondary electron imaging at high temperature. The nanotubes were first imaged at room temperature under high vacuum ( $\sim 10^{-4}$  Pa), and then the sample was heated at 50 °C/min under vacuum. When the temperature reached 300 °C, a heat shield with electrostatic bias was introduced between the sample and the electron column in order to protect the column.  $\text{O}_2$  was introduced into the chamber when the sample temperature was stabilized to the desired oxidizing temperature. During oxidation, images were recorded sequentially (4-10 sec per frame) under 11 Pa of  $\text{O}_2$  using the optimized beam energy of 1.8 kV, spot size of 5, emission current of 150  $\mu\text{A}$  and working distance of 20 mm. Note that the beam energy used in our experiments is well below the knock-on displacement energy of carbon atoms in SWCNTs.<sup>47,48</sup> Sample temperature was measured by a home-made thermocouple placed just below the sample. The temperature accuracy for each heating stage was verified by checking the fusion temperature of a small gold wire.

**Conflict of Interest:** The authors declare no competing financial interest.

**Supporting Information Available:** Oxidation behavior of SWCNTs extracted from coupled SEM-AFM experiments. SEM images of the nanotubes before, after and during oxidation at different temperatures. Number, position, frequency and reactivity of cutting of the nanotubes extracted from oxidation experiments at four different temperatures. Relation among number of cutting, time of exposure to oxygen and reactivity of individual SWCNTs. Comparison of the reactivity of metallic and semiconducting SWCNTs. Oxidation behavior of Raman pre-characterized sample. Contrast fluctuation along the length of individual nanotubes. Effect of prolonged electron beam exposure on nanotube oxidation. This material is available free of charge via the internet at <http://pubs.acs.org>.

**Acknowledgement.** Support from AFOSR and EOARD (contract FA8655-12-1-2059) is gratefully acknowledged.

## References

1. Dean, K. A.; Chalamala, B. R. The Environmental Stability of Field Emission from Single-Walled Carbon Nanotubes. *Appl. Phys. Lett.* **1999**, *75*, 301763019.
2. Bonard, J.-M.; Maier, F.; Stöckli, T.; Châtelain, A.; de Heer, W. A.; Salvetat, J.-P.; Forró, L. Field Emission Properties of Multiwalled Carbon Nanotubes. *Ultramicroscopy* **1998**, *73*, 7615.
3. Futaba, D. N.; Hata, K.; Yamada, T.; Mizuno, K.; Yumura, M.; Iijima, S. Kinetics of Water-Assisted Single-Walled Carbon Nanotube Synthesis Revealed by a Time-Evolution Analysis. *Phys. Rev. Lett.* **2005**, *95*, 056104.
4. Nasibulin, A. G.; Brown, D. P.; Queipo, P.; Gonzalez, D.; Jiang, H.; Kauppinen, E. I. An Essential Role of CO<sub>2</sub> and H<sub>2</sub>O during Single-Walled CNT Synthesis from Carbon Monoxide. *Chem. Phys. Lett.* **2006**, *417*, 1796184.
5. Yu, B.; Liu, C.; Hou, P.; Tian, Y.; Li, S.; Liu, B.; Li, F.; Kauppinen, E. I.; Cheng, H. Bulk Synthesis of Large Diameter Semiconducting Single-Walled Carbon Nanotubes by Oxygen-Assisted Floating Catalyst Chemical Vapor Deposition. *J. Am. Chem. Soc.* **2011**, *133*, 523265235.

6. Dillon, A. C.; Gennett, T.; Jones, K. M.; Alleman, J. L.; Parilla, P. A.; Heben, M. J. A Simple and Complete Purification of Single-Walled Carbon Nanotube Materials. *Adv. Mater.* **1999**, *11*, 135461358.
7. Wiltshire, J. G.; Khlobystov, A. N.; Li, L. J.; Lyapin, S. G.; Briggs, G. A. D.; Nicholas, R. J. Comparative Studies on Acid and Thermal Based Selective Purification of HiPCO Produced Single-Walled Carbon Nanotubes. *Chem. Phys. Lett.* **2004**, *386*, 2396243.
8. Zhang, G.; Mann, D.; Zhang, L.; Javey, A.; Li, Y.; Yenilmez, E.; Wang, Q.; McVittie, J. P.; Nishi, Y.; Gibbons, J.; et al. Ultra- High-Yield Growth of Vertical Single-Walled Carbon Nanotubes: Hidden Roles of Hydrogen and Oxygen. *Proc. Natl. Acad. Sci. U.S.A.* **2005**, *102*, 16141616145.
9. Xu, Y.; Peng, H.; Hauge, R. H.; Smalley, R. E. Controlled Multistep Purification of Single-Walled Carbon Nanotubes. *Nano Lett.* **2005**, *5*, 1636168.
10. Chen, Z.; Ziegler, K. J.; Shaver, J.; Hauge, R. H.; Smalley, R. E. Cutting of Single-Walled Carbon Nanotubes by Ozonolysis. *J. Phys. Chem. B* **2006**, *110*, 11624611627.
11. Yu, B.; Hou, P.; Li, F.; Liu, B.; Liu, C.; Cheng, H. Selective Removal of Metallic Single-Walled Carbon Nanotubes by Combined in Situ and Post-Synthesis Oxidation. *Carbon* **2010**, *48*, 294162947.
12. Chiang, I. W.; Brinson, B. E.; Huang, A. Y.; Willis, P. A.; Bronikowski, M. J.; Margrave, J. L.; Smalley, R. E.; Hauge, R. H. Purification and Characterization of Single-Wall Carbon Nanotubes (SWNTs) Obtained from the Gas-Phase Decomposition of CO (HiPco Process). *J. Phys. Chem. B* **2001**, *105*, 829768301
13. Ajayan, P.M.; Ebbesen, T.W.; Ichihashi, T.; Iijima, S.; Tanigaki, K.; Hiura, H. Opening Carbon Nanotubes with Oxygen and Implications for Filling. *Nature* **1993**, *362*, 5226525.
14. Tsang, S. C.; Harris, P. J. F.; Green, M. L. H. Thinning and Opening of Carbon Nanotubes by Oxidation Using Carbon Dioxide. *Nature* **1993**, *362*, 5206522.
15. Dresselhaus, M. S.; Dresselhaus, G.; Eklund, P. C., Chapter 1- Historical Introduction. **1996**, 1-14.
16. Saito, R.; Dresselhaus, G.; Dresselhaus, M. S.; Others, Physical properties of carbon nanotubes. Imperial College Press London: 1998; Vol. 3.
17. Cao, Q.; Rogers, J. A. Ultrathin Films of Single-Walled Carbon Nanotubes for Electronics and Sensors: A Review of Fundamental and Applied Aspects. *Adv. Mater.* **2008**, *21*, 29653.

18. Gabor, N. M.; Zhong, Z. H.; Bosnick, K.; Park, J.; McEuen, P. L. Extremely Efficient Multiple Electron-Hole Pair Generation in Carbon Nanotube Photodiodes. *Science* **2009**, *325*, 1367–1371.

19. Allen, B. L.; Kichambare, P. D.; Star, A. Carbon Nanotube Field-Effect-Transistor-Based Biosensors. *Adv. Mater.* **2007**, *19*, 14396–1451.

20. Burghard, M.; Klauk, H.; Kern, K. Carbon-Based Field-Effect Transistors for Nanoelectronics. *Adv. Mater.* **2009**, *21*, 2586–2600.

21. Lolli, G.; Zhang, L.; Balzano, L.; Sakulchaicharoen, N.; Tan, Y.; Resasco, D. E. Tailoring (n,m) Structure of Single-Walled Carbon Nanotubes by Modifying Reaction Conditions and the Nature of the Support of CoMo Catalysts. *J. Phys. Chem. B* **2006**, *110*, 21086–2115.

22. Li, X. L.; Tu, X.; Zaric, S.; Welsher, K.; Seo, W. S.; Zhao, W.; Dai, H. Selective Synthesis Combined with Chemical Separation of Single-Walled Carbon Nanotubes for Chirality Selection. *J. Am. Chem. Soc.* **2007**, *129*, 15770–15771.

23. Miyata, Y.; Kawai, T.; Miyamoto, Y.; Yanagi, K.; Maniwa, Y.; Kataura, H. Chirality-Dependent Combustion of Single-Walled Carbon Nanotubes. *J. Phys. Chem. C* **2007**, *111*, 9671–9677.

24. Wiltshire, J. G.; Khlobystov, A. N.; Li, L. J.; Lyapin, S. G.; Briggs, G. A. D.; Nicholas, R. J. Comparative Studies on Acid and Thermal Based Selective Purification of HiPCO Produced Single-Walled Carbon Nanotubes. *Chem. Phys. Lett.* **2004**, *386*, 2396–243.

25. Borowiak-Palen, E.; Pichler, T.; Liu, X.; Knupfer, M.; Graff, A.; Jost, O.; Pompe, W.; Kalenczuk, R. J.; Fink, J. Reduced Diameter Distribution of Single-Wall Carbon Nanotubes by Selective Oxidation. *Chem. Phys. Lett.* **2002**, *363*, 5676–572.

26. Chiang, I. W.; Brinson, B. E.; Huang, A. Y.; Willis, P. A.; Bronikowski, M. J.; Margrave, J. L.; Smalley, R. E.; Hauge, R. H. Purification and Characterization of Single-Wall Carbon Nanotubes (SWNTs) Obtained from the Gas-Phase Decomposition of CO (HiPco Process). *J. Phys. Chem. B* **2001**, *105*, 8297–8301.

27. Nagasawa, S.; Yudasaka, M.; Hirahara, K.; Ichihashi, T.; Iijima, S. Effect of Oxidation on Single-Wall Carbon Nanotubes. *Chem. Phys. Lett.* **2000**, *328*, 3746–380.

28. Zhou, W.; Zhan, S.; Ding, L.; Liu, J. General Rules for Selective Growth of Enriched Semiconducting Single Walled Carbon Nanotubes with Water Vapor as in Situ Etchant. *J. Am. Chem. Soc.* **2012**, *134*, 140196–14026.

29. Zhang, G.; Qi, P.; Wang, X.; Lu, Y.; Li, X.; Tu, R.; Bangsaruntip, S.; Mann, D.; Zhang, L.; Dai, H. Selective Etching of Metallic Carbon Nanotubes by Gas-Phase Reaction. *Science* **2006**, *314*, 9746977.

30. Yang, C.; An, K. H.; Park, J. S.; Park, K. A.; Lim, S. C.; Cho, S.; Lee, Y. S.; Park, W.; Park, C. Y.; Lee, Y. H. Preferential Etching of Metallic Single-Walled Carbon Nanotubes with Small Diameter by Fluorine Gas. *Phys. Rev. B* **2006**, *73*, 075419.

31. Zhou, W.; Zhan, S.; Ding, L.; Liu, J. General Rules for Selective Growth of Enriched Semiconducting Single Walled Carbon Nanotubes with Water Vapor as in Situ Etchant. *J. Am. Chem. Soc.* **2012**, *134*, 14019614026.

32. Zhang, H.; Liu, Y.; Cao, L.; Wei, D.; Wang, Y.; Kajiura, H.; Li, Y.; Noda, K.; Luo, G.; Wang, L.; et al. A Facile, Low-Cost, and Scalable Method of Selective Etching of Semiconducting Single-Walled Carbon Nanotubes by a Gas Reaction. *Adv. Mater.* **2009**, *21*, 8136816.

33. Miyata, Y.; Maniwa, Y.; Kataura, H. Selective Oxidation of Semiconducting Single-Wall Carbon Nanotubes by Hydrogen Peroxide. *J. Phys. Chem. B* **2006**, *110*, 25629.

34. Hodge, S. A.; Bayazit, M. K.; Coleman, K. S.; Shaffer, M. S. P. Unweaving the Rainbow: A Review of the Relationship between Single-Walled Carbon Nanotube Molecular Structures and their Chemical Reactivity. *Chem. Soc. Rev.* **2012**, *41*, 440964429.

35. Kawai, T.; Miyamoto, Y. Chirality-Dependent C-C Bond Breaking of Carbon Nanotubes by Cyclo-Addition of Oxygen Molecule. *Chem. Phys. Lett.* **2008**, *453*, 2566261.

36. Moon, C.; Kim, Y.; Lee, E.; Jin, Y.; Chang, K. J. Mechanism for Oxidative Etching in Carbon Nanotubes. *Phys. Rev. B* **2002**, *65*, 155401.

37. An, K. H.; Park, J. S.; Yang, C.; Jeong, S. Y.; Lim, S. C.; Kang, C.; Son, J.; Jeong, M. S.; Lee, Y. H. A Diameter-Selective Attack of Metallic Carbon Nanotubes by Nitronium Ions. *J. Am. Chem. Soc.* **2005**, *127*, 519665203.

38. Ye, J. T.; Tang, Z. K. Raman Spectra and Thermal Stability Analysis of 0.4nm Freestanding Single-Walled Carbon Nanotubes. *Phys. Rev. B* **2005**, *72*, 045414.

39. Kroes, J. M. H.; Pietrucci, F.; Curioni, A.; Jaafar, R.; Gröning, O.; Andreoni, W. Atomic Oxygen Chemisorption on Carbon Nanotubes Revisited with Theory and Experiment. *J. Phys. Chem. C* **2013**, *117*, 194861954.

40. Doyle, C. D.; Rocha, J. R.; Weisman, R. B.; Tour, J. M. Structure-Dependent Reactivity of Semiconducting Single-Walled Carbon Nanotubes with Benzenediazonium Salts. *J. Am. Chem. Soc.* **2008**, *130*, 6795–6800.

41. Yamamoto, M.; Einstein, T. L.; Fuhrer, M. S.; Cullen, W. G. Charge Inhomogeneity Determines Oxidative Reactivity of Graphene on Substrates. *ACS Nano* **2012**, *6*, 8335–8341.

42. Kocabas, C.; Hur, S.-H.; Gaur, A.; Meitl, M. A.; Shim, M.; Rogers, J. A. Guided Growth of Large-Scale, Horizontally Aligned Arrays of Single-Walled Carbon Nanotubes and Their Use in Thin-Film Transistors. *Small* **2005**, *1*, 1110–1116.

43. Zhang, L.; Gao, F.; Huang, S. The imaging Mechanism of Single-Walled Carbon Nanotubes on Si/SiO<sub>2</sub> Wafer in Scanning Electron Microscopy. *J. Microsc.* **2011**, *241*, 188–194.

44. Li, J.; He, Y.; Han, Y.; Liu, K.; Wang, J.; Li, Q.; Fan, S.; Jiang, K. Direct Identification of Metallic and Semiconducting Single-walled Carbon Nanotubes in Scanning Electron Microscope. *Nano Lett.* **2012**, *12*, 4095–4101.

45. Javey, A.; Guo, J.; Paulsson, M.; Wang, Q.; Mann, D.; Lundstrom, M.; Dai, H. J. High-Field Quasiballistic Transport in Short Carbon Nanotubes. *Phys. Rev. Lett.* **2004**, *92*, 106804.

46. Javey, A.; Guo, J.; Farmer, D. B.; Wang, Q.; Yenilmez, E.; Gordon, R. G.; Lundstrom, M.; Dai, H. J. Self-Aligned Ballistic Molecular Transistors and Electrically Parallel Nanotube Arrays. *Nano Lett.* **2004**, *4*, 1319.

47. Smith, B. W.; Luzzi, D. E. Electron Irradiation Effects in Single Wall Carbon Nanotubes. *J. Appl. Phys.* **2001**, *90*, 3509–3515.

48. Warner, J. H.; Schäffel, S.; Zhong, G.; Rümmeli, M. H.; Büchner, B.; Robertson, J.; Briggs, G. A. D. Investigating the Diameter-Dependent Stability of Single-Walled Carbon Nanotubes. *ACS Nano* **2009**, *3*, 1557–1563.

49. Raua, E. I.; Fakhfakh, S.; Andrianova, M. V.; Evstafeva, E. N.; Jbarab, O.; Rondotb, S.; Mouzeb, D. Second Crossover Energy of Insulating Materials Using Stationary Electron Beam under Normal Incidence. *Nucl. Instrum. Methods Phys. Res., Sect. B* **2008**, *266*, 7196–729.

50. Joo, J.; Chow, B. Y.; Joseph M. Jacobson, J. M. Patterning on Insulating Substrates by Critical Energy Electron Beam Lithography. *Nano Lett.* **2006**, *6*, 2021–2015.

51. Li, J.; He, Y.; Han, Y.; Liu, K.; Wang, J.; Li, Q.; Fan, S.; Jiang, K. Direct Identification of Metallic and Semiconducting Single-walled Carbon Nanotubes in Scanning Electron Microscope. *Nano Lett.* **2012**, *12*, 4095–4101.

52. Liu, Li.; Ryu, S.; Tomasik, M. R.; Stolyarova, E.; Jung, N.; Hybertsen, M. S.; Steigerwald, M. L.; Brus, L. E.; Flynn, G. W. Graphene Oxidation: Thickness-Dependent Etching and Strong Chemical Doping. *Nano lett.* **2008**, 8, 1965-1970.

53. Martin, J.; Akerman, N.; Ulbricht, G.; Lohmann, T.; Smet, J. H.; von Klitzing, K.; Yacoby, A. Observation of Electron-Hole Puddles in Graphene Using a Scanning Single-Electron Transistor. *Nat. Phys.* **2008**, 4, 1446-148.

54. Zhang, Y.; Brar, V. W.; Girit, C.; Zettl, A.; Crommie, M. F. Origin of Spatial Charge Inhomogeneity in Graphene. *Nat. Phys.* **2009**, 5, 722-726.

55. Deal, B. E. Standardized Terminology for Oxide Charges Associated with Thermally Oxidized Silicon. *J. Electrochem. Soc.* **1980**, 127, 979-981.

56. Mack, Sebastian et al "Silicon Surface Passivation by Thin Thermal Oxide/PECVD Layer Stack Systems," *Photovoltaics, IEEE* ,2011, 1, pp.135,145

57. Chuang, C-H.; Sow, C-H.; Lin, M-T. Spectro-Microscopic Study of Laser Modified Carbon Nanotubes. In *Electronic Properties of Carbon Nanotubes*; Marulanda, J. M., Eds.; In Tech: Shanghai, 2011; pp 247-266.

58. Schneider, G. F.; Calado, V. E.; Zandbergen, H.; L. M. K. Vandersypen, L. M. K.; Dekker, C. Wedging Transfer of Nanostructures. *Nano lett.* **2010**, 10, 1912-1916.